NASA-CR-202160

Final NASAReport
Grant No. NCC 2-718

Electron-Beam Diagnostic Methods for Hypersonic Flow Diagnostics.

prepared by

University of California at San Diego

Center for Energy and Combustion Research

Mail Code 0411
La Jolla, Ca 92093
tel: (619) 534-2433
fax: (619) 534-5354

January 20, 1994

TABLE OF CONTENTS

Abstract

The purpose of this work was the evaluation of the use of electron-bean fluorescence for flow measurements during hypersonic flight. Both analytical and numerical models were developed in this investigation to evaluate quantitatively flow field imaging concepts based upon the electron beam fluorescence technique for use in flight research and wind tunnel applications. Specific models were developed for: (1) fluorescence excitation/emission for nitrogen, (2) rotational fluorescence spectrum for nitrogen, (3) single and multiple scattering of electrons in a variable density medium, (4) spatial and spectral distribution of fluorescence, (5) measurement of rotational temperature and density, (6) optical filter design for fluorescence imaging, (7) and temperature accuracy and signal acquisition time requirements. Application of these models to a typical hypersonic wind tunnel flow is presented. In particular, the capability of simulating the fluorescence resulting from electron impact ionization in a variable density nitrogen or air flow provides the capability to evaluate the design of imaging instruments for flow field mapping.

The results of this analysis is a recommendation that quantitative measurements of hypersonic flow fields using electron-bean fluorescence is a tractable method with electron beam energies of 100 keV. With lower electron energies, electron scattering increases with significant beam divergence which makes quantitative imaging difficult. The potential application of the analytical and numerical models developed in this work is in the design of an flow field imaging instrument for use in hypersonic wind tunnels or onboard a flight research vehicle.

1.0 Model of Electron Beam Fluorescence Excitation/Emission Process

A gas molecule can be excited from its electronic ground state to higher electronic states that fluoresce as a result of the interaction with a moving electron. Electron-beam fluorescence spectroscopy was demonstrated by Muntz in the context of low-density wind tunnel applications in the 1960's. Muntz's review [1] provides an excellent summary of the early development of the technique. Further development and applications of the technique from the early 1970's to the present are found in a variety of applied physics journals and most notably in the publications of the proceedings of the Rarefied Gas Dynamics Symposia [2]. The most recent review of the technique was presented at a lecture series on measurement techniques for hypersonic flow [3]. A comparison of the electron-beam fluorescence technique with other optical methods for hypersonic applications is available in a recent NATO/AGARD review [4].

Electron-beam fluorescence from nitrogen has been used extensively to measure gas density and rotational temperature, and is the still the most useful approach for hypersonic flows studies in wind tunnel and flight experiments. At low density ($n < 10^{17}$ cm^{-3}), fluorescence from the B $^2\Sigma$-X $^2\Sigma$ transition of N_2^+ at 390-480 nm (first-negative system) has been used most often. For moderately fast electrons (>1 keV), it is possible to model the excitation process for the first-negative system and to relate the observed spectrum of the excited-state fluorescence to gas properties such as density, rotational and vibrational temperature, and velocity. To illustrate the physics involved in electron-beam fluorescence from nitrogen, **Figure 1** shows a schematic diagram of the processes that are involved.

In the electron beam, a fast electron interacts with the X $^1\Sigma$ ground state of the nitrogen molecule, exciting it to vibrational levels in the B $^2\Sigma$ state of the nitrogen ion. This process can be described for a specific vibrational level, v"=0, in the ground state of the neutral molecule and a specific vibrational level, v'=0, in the excited state of the ion by:

$$e^- + N_2\left[X^1\Sigma(v''=0)\right] \xrightarrow{W_{00}} N_2^+\left[B^2\Sigma(v'=0)\right] + e^- + e_s^+ \qquad (1a)$$

$$W_{00} = n_e v_e E_{00}(v_e) \qquad (1b)$$

where the rate of excitation from v"=0 to v'=0, W_{00}, can be calculated from the electron number density n_e, the electron velocity v_e, and the excitation cross section E_{00}. At high densities

($>10^{16}$ cm^{-3}), the secondary electron, e_s^-, produced in the ionization can contribute to the fluorescence-excitation process.

After electron-beam excitation, the nitrogen ion in the $B\,^2\Sigma$ (v'=0) state radiates to the $X\,^2\Sigma$ (v"=0) state, emitting a photon of energy hv at the spontaneous emission rate, A_{00}:

$$N_2^+\left[B^2\Sigma(v'=0)\right] \xrightarrow{A_{00}} N_2^+\left[X^2\Sigma(v''=0)\right] + h\upsilon \tag{2}$$

Collisions with the background gas, M, can depopulate the excited state of the ion by so-called "electronic quenching," and result in a loss of signal:

$$N_2^+\left[B^2\Sigma(v'=0)\right] + M \xrightarrow{Q_0} N_2^+\left[X^2\Sigma(v''=0)\right] + M^* \tag{3a}$$

$$Q_0 = n_g v_g \sigma_0(v_g) \tag{3b}$$

where the rate of electronic quenching, Q_0, can be calculated from the gas density n_g, the relative collision velocity v_g, and the quenching cross section $\sigma_0(v_g)$. Other depopulation processes related to the direct removal of the nitrogen ion, such as dissociative recombination and charge exchange with molecular oxygen, take place on a time scale much longer than the radiative emission and do not have to be included in the analysis.

Based on the description of the electron-beam fluorescence process outlined in Eqs. (1)-(3), the expected signal level from the N_2^+ (0,0) band as a function of the molecular nitrogen density can be calculated from a two-level excitation-emission model. A photometric equation describing the detected signal P (photon counts/s) from a source of brightness B_λ (photons s^{-1} cm^{-2} $ster^{-1}$) with a detector of area A_d and detection quantum efficiency h_d from an optical collection system with solid angle W and collection efficiency η_{os} can be described:

$$P = B_\lambda A_d \eta_d \Omega \eta_{os} \tag{4}$$

The fluorescent brightness from the N_2^+ (0,0) band is proportional to the gas density, N_g, and can be calculated from the steady-state volumetric emission rate for excitation by a cylindrical electron beam of diameter d:

$$B_\lambda = \left(\frac{A_{00}}{1/\tau_{rad} + Q_0} \right) W_\infty n_g \frac{d}{16} \tag{5}$$

where τ_{rad} is the radiative lifetime of the B $^2\Sigma$ (v'=0) state. The solid angle W of a light collection system to gather the fluorescence emission is related to its f number (f/#):

$$\Omega = \frac{\pi}{4(f/\#)^2} \tag{6}$$

Combining the preceding relationships, the photometric equation can be expressed as:

$$P = I E_{00} n_g \left(\frac{A_{00}}{1/\tau_{rad} + Q_0} \right) \frac{A_d \eta_d \eta_{os}}{16 de (f/\#)^2} \tag{7}$$

Note that the photometric throughput is directly proportional to the electron-beam current I, the gas density n_g, and the efficiencies of the optical system and detector, and it is inversely proportional to the square of the f/#. The electron charge is e. Equation (7) is the basis for the estimation of the electron-beam excited fluorescence signal from a uniform diameter electron beam propagating into a gas at a known number density.

To evaluate the capability of an electron-beam fluorescence diagnostics instrument in a hypersonic flow facility we can predict the expected signal level using equation (7) and typical operating characteristics for a 10 mA electron beam operating with electron energies of 10 keV, 20 keV, and 50 keV. The parameters to be used in equation (7) to predict the photometric signal are given in table I.

Table I. Parameter values for photometric equation to calculate electron beam fluorescence signal from the from $N_2^+(0,0)$ band of the $B\,^2\Sigma$ -$X\,^2\Sigma$ transition .

electron-beam current, I	10 mA
excitation cross section, E_{00}	1.500×10^{-18} cm^2
(10 keV, 20 keV,and 50 keV)	0.976×10^{-18} cm^2
	0.510×10^{-18} cm^2
spontaneous emission rate, A_{00}	1.24×10^{7} sec^{-1}
radiative life time t_{rad}	66 nsec
detector area, A_d	0.001 cm^2
detector quantum efficiency, η_d	0.20
optical system efficiency, η_{os}	0.15
optical system, f/#	f/20
electron beam diameter, d	1 mm

Using values of the parameters given in table I for a proposed wind tunnel instrument, the time required to collect sufficient signal from the electron beam fluorescence to maintain a signal-to-noise-ratio of 100 in a density measurement is plotted in **Figure 2** as a function of gas density and electron beam energy.

The three curves that are plotted in **Figure 2** show the increase in signal acquisition as the electron beam energy is changed from 10, 20, and 50 keV. The longer signal acquisition time is the result of the decrease in the excitation cross section E_{00} with increasing beam voltage V_{eb}; $E_{00} \sim (V_{eb} / \ln V_{eb})^{-1}$. For all three electron beam energies the time required to measure the gas density with a signal-to-noise ratio of 100 is less than 100 millisecond for gas densities greater than 10^{14} cm^{-3}. Operating the beam at 50 keV would provide the best spatial resolution, however a factor of two loss in signal strength would accompany this increased spatial resolution and would therefore require an increase in signal acquisition time to maintain the same signal-to-noise ratio. To measure the nitrogen rotational temperature from the electron-beam fluorescence with the equivalent signal-to-noise ratio would increase the signal acquisition time by a factor of 100 [5].

To determine the signal level and the spatial resolution that can be obtained in the development of an electron-beam fluorescence instrument for application to a hypersonic wind tunnel model the distribution of gas flow properties in a typical facility is necessary for system design and analysis. We have used pitot probe measurements of the Mach number, pressure, density, and temperature across a Mach 12 nozzle at a stagnation temperature of 1066 K and a stagnation pressure of 54.4 atm. The data was provided in English units and were converted to

cgs units for use in the analysis of the fluorescence signal level and electron beam propagation characteristics that determine spatial resolution. In **Figures 3-6** the Mach number, temperature, density (mass units), and density (number density) distribution across the Mach 12 nozzle are plotted.

In **Figure 3** the Mach number distribution is relatively uniform at M=12.2 across the central 60 per cent of the flow out to a radial distance of 15 cm. Beyond the uniform core boundary layer effects at the edge of the jet drop the Mach number down to sonic conditions. The temperature distribution in **Figure 4** follows the Mach distribution with a uniform core temperature of 34 K over the central 30 cm core of the nozzle. The density distributions in Figs. 5 and 6 are more sensitive to Mach number variation than the temperature and shows this in the central 30 cm core. The number density distribution in the flow range from 10^{16} to 10^{17} cm^{-3}. This density can be used along with the signal calculation in **Figure 2** to determine minimum signal acquisition time for the operation of an electron beam fluorescence instrument in this flow. At the density in the core of the Mach 12 flow signal acquisition times less than 1 millisecond are sufficient to obtain a SNR of 100 for a density measurement. The flow properties in Figs. 3-6 have been least square fit to polynomial functions for use in the modeling of a fluorescence imaging instrument and the prediction of electron beam propagation.

2.0 Measurement of Gas Properties in Hypersonic Flows

A computer model for the prediction of the rotational fluorescence spectrum to be expected from nitrogen at specified rotational temperature has been developed, also a model for the measurement of nitrogen density and rotational temperature using band pass filters has been developed.

2.1 A Model for the Rotational Fluorescence Spectrum from Nitrogen.

Rotational spectra are useful to gas dynamics in that the information contained in these spectra can be used to determine the rotational temperature of the gas. This has important applications in rarefied gas dynamics, advanced propulsion diagnostics, and many others. Much research has been done regarding rotational spectra applicable to gas dynamics, especially for the nitrogen first-negative transition ($N_2^+B\ ^2\Sigma_u^+ \rightarrow N_2^+X\ ^2\Sigma_g^+$). Most of this research has utilized the Electron-Beam Fluorescence technique (EBF). In EBF, an energetic beam of electrons is injected into the gas, causing the loss of a nitrogen molecule electron to create the nitrogen ion N_2^+. This ion undergoes further transitions, including rotational transitions which produce the rotational spectra of interest in this study. Through selection rules and transition probabilities, it is possible to theoretically model rotational spectra. Application of this theory will be presented in more detail under section **4.4**.

The theoretical model for the first negative bands of the nitrogen ion is given here, although similar analyses can be done for other diatomic or polyatomic molecules with a permanent dipole moment. In the application of Electron Beam Fluorescence (EBF) to nitrogen, $N_2X\ ^1\Sigma_g^+$ ground state molecules are ionized and excited to the $N_2^+B\ ^2\Sigma_u^+$ state through inelastic collisions with high energy electrons. The resulting fluorescence of the $N_2^+B\ ^2\Sigma_u^+ \rightarrow N_2^+X\ ^2\Sigma_g^+$ transition is then observed, which includes rotational transitions between these two states. Hereafter, an upper rotational state of the N_2^+ ion will have a single prime ('), while the lower rotational state will have two primes ("). The $N_2X\ ^1\Sigma_g^+$ ground state nitrogen molecule will have three primes for its rotational state.

We assume that dipole selection rules are applicable and therefore rotational transitions only occur for $\Delta K = \pm 1$, where K is the rotational quantum number. As a convention, $\Delta K = -1$ corresponds to a R-branch transition and $\Delta K = +1$ corresponds to a P-branch transition. Thus, a

$K+1 \rightarrow K$ transition is part of the R-branch of the observed spectra, and a $K-1 \rightarrow K$ transition is part of the P-branch.

With each rotational state there is a corresponding energy of that state. A *term value*, denoted by *F(K)*, is the energy associated with rotational state K divided by hc, where h is Planck's constant and c is the speed of light, resulting in *F(K)* having units of wavenumber.

$$F(K) = \frac{E(K)}{hc} = \frac{h}{8\pi^2 I} K(K+1) = B \cdot K(K+1) \tag{8}$$

Term values also depend on the vibrational state of the molecule. When this correction is taken into account, the subscript n is added, i.e. $F_v(K) = B_v K(K+1)$. The wavenumbers at which transitions occur depend on the energy of the transition and therefore the term values associated with these energies. For R-branch transitions we have

$$\bar{\nu} = \overline{\nu_0} + F_v'(K'+1) - F_v''(K') \tag{9}$$

and for P-branch transitions

$$\bar{\nu} = \overline{\nu_0} + F_v'(K'-1) - F_v''(K') \tag{10}$$

where $\overline{\nu_0}$ is the vibrational band origin of the rotational spectra ($\overline{\nu_0}$ = 25566.0 cm^{-1})for the nitrogen (0,0) vibrational band), F_v' is the upper state term value, F_v'' is the lower state term value, and K' is the lower state rotational quantum number.

Inserting equation (1) into (2) & (3) we find

$$\bar{\nu} = \overline{\nu_0} + 2B_v' + (3B_v' - B_v'')K' + (B_v' - B_v'')K'^2 \qquad \text{R-branch} \tag{11}$$

$$\bar{\nu} = \overline{\nu_0} + (B_v' + B_v'')K' + (B_v' - B_v'')K'^2 \qquad \text{P-branch} \tag{12}$$

An approximation can be made to account for the vibrational dependence of B_v on the vibrational quantum number through

$$B_v = B_e - a_e(v + 1/2) \tag{13}$$

where B_e is the hypothetical equilibrium state of the molecule, a_e is a vibration-rotation constant, and v is the vibrational quantum number. For nitrogen-ion transition $v = 0$, and for B_e , a_e , and $\overline{\nu_0}$ we use the following values:

$$B_v' = B_e' - a_e'(v+1/2) = 2.083 - .0195(1/2) = \underline{2.07325} \text{ cm}^{-1} \quad (14)$$

$$B_v'' = B_e'' - a_e''(v+1/2) = 1.932 - .0200(1/2) = \underline{1.92200} \text{ cm}^{-1} \quad (15)$$

With equations (11) & (12), the wavenumbers of transitions are known as a function of rotational quantum number K'. This defines the x-axis of the rotational spectra.

The intensity of a transition is related to the Boltzmann population distribution

$$N_{K''} \sim \sigma(2K''+1)\exp\left\{\frac{K''(K''+1)\Theta}{T_r}\right\} \quad (16)$$

where $N_{K''}$ is the number of molecules in the ground $N_2X\ ^1S_g^+$ state with rotational quantum number K'', T_r is the rotational temperature, and $\Theta = 2.878$ K is the rotational constant for the ground state. σ is a factor which equals 1 for odd quantum numbers of K'' and equals 2 for even quantum numbers due to nuclear spin degeneracy. The rate of excitation will be proportional to $K''/(2K''+1)$ for P-branch transitions (i.e. $K' = K''-1$), and proportional to $(K''+1)/(2K''+1)$ for R-branch transitions (i.e. $K' = K''+1$). Thus,

$$R(K') \sim \left(\frac{K'}{2K'-1}\right)N_{K'-1} + \left(\frac{K'+1}{2K'+3}\right)N_{K'+1} \quad (17)$$

where $R(K')$ is the rate of excitation into the K' rotational level of $N_2^+B\ ^2\Sigma_u^+$ and the excitation factors have been written in terms of K'. The resulting intensity from this K' rotational line will be split between the P and R branches and is proportional to $R(K')$,

$$I_{K'} \sim \left(\frac{P_{K'}}{2K'+1}\right)R(K') \quad (18)$$

where $P_{K'} = \begin{cases} K' & \text{for the R - branch transition} \\ K'+1 & \text{for the P - branch transition} \end{cases}$

Combining eqs. (9), (10), & (11) together, we obtain the equation for the theoretical intensity as a function of K'

$$\frac{I_{K'}}{\sigma} \sim P_{K'} \cdot G(K', T_r) \exp\left\{\frac{-K'(K'+1)\Theta}{T_r}\right\} \tag{19}$$

where

$$G(K', T_r) = \frac{K' \exp\left\{\frac{2K'\Theta}{T_r}\right\} + (K'+1)\exp\left\{\frac{-2(K'+1)\Theta}{T_r}\right\}}{2K'+1} \tag{20}$$

Now wavelength and intensity are both known as a function of upper state rotational quantum number K' through eqs. (4), (5), (12) & (13). Thus, theoretical plots of rotational spectra can be calculated as shown in figs 7a-f. However, equation (12) is a proportionality equation. A normalization is obtained by using a reference rotational temperature, and then normalizing intensities of different rotational temperatures with the maximum resulting intensity of the reference temperature. In this study, the rotational reference temperature used was 300 K. As seen in **Figures 7(a)-(f)**, more rotational states are excited as temperature is increased while intensity of low quantum number (high wavelength) transitions decay. Thus, in **Figure 7(a)** at 40 K there are only a few appreciably excited rotational states, but those that are excited have relatively high intensities, yet in **Figure 7(f)** at 1000 K the converse is true. Also, note that at higher temperatures the P-branch lines start to interfere with the R-branch. This is an inherent problem with spectroscopic methods, but will not be a significant factor in the filter analysis.

3.0 Modeling of Beam Scattering

An evaluation of two earlier analyses of beam divergence due to electron scattering was made to assess their application to hypersonic wind tunnel flows. Based on this assessment, the need became evident to model the effects of high gas density on beam propagation and to model beam gas interactions at significantly higher energies. Thus a model combining single and multiple scattering models was developed that well approximates previous models in both the thin and dense gas flow limits, and bridges these limits for flows that are transitional in the context of mean scatterings per electron.

3.1 Non-relativistic Electron-beam Envelope Model.

One useful measure of an e-beam's radial dimension is its "root-mean-square" radius, defined as a function of axial distance, z, from the beam gun aperture:

$$R_{rms}(z) = \left(\frac{\int_0^\infty n_e(r,z) r^2 dr}{\int_0^\infty n_e(r,z) dr} \right)^{1/2} \tag{21}$$

where n_e is the beam electron number density.

For comparison with the beam divergence data, the envelope model of Lee and Cooper[17] based on the assumption of self-similar radial expansion was modified to account for electron-gas interactions ranging from single- to multiple-scattering regimes. Relativistic effects in the Lee-Cooper analysis were not included. The modified model predicts a normalized rms radius is given by

$$\left(\frac{R_{rms}(s)}{R_{rms}(s=0)} \right)^2 = 1 + \frac{2}{sR} \left(1 - s + \frac{1}{2}s^2 + \frac{1}{24}s^4 - e^{-s} \right) \langle \theta_s^2 \rangle \tag{22}$$

where

$$\langle \theta_s^2 \rangle = \frac{\int \theta^2 \frac{d\sigma}{d\Omega} d\Omega}{\int \frac{d\sigma}{d\Omega} d\Omega} \tag{23}$$

is the mean square single scattering angle, $s_R = n_g \sigma R_{rms}(s=0)$ is a non-dimensional scaling parameter, $d\sigma/d\Omega$ is the total differential scattering cross section, σ is the non-dimensional target thickness, $n_g \sigma z$, n_g is the gas number density, and σ is the total scattering cross-section, defined as the denominator in (23). Note that the first four terms of the polynomial bracketed on the right hand side of (22) are cancelled by terms in the expansion for e^{-s}, so that for $s << 1$ (no scattering limit), the mean square radius is proportional to $(1+\varepsilon s^3)$ along the beam. For $s >> 1$ (scattering dominated limit), the right-hand-side is dominated by the fifth degree term on the right hand side. Both extremes are well approximated by (22), using the authors' proposed bridging function, e^{-s}. and both extremes are consistent with single and multiple scattering representations of the Lee model, subject to an assumed linear energy transfer rate between beam and gas over the length of the beam.

Interpretation of the Lee model remains subject to the uncertainty in the definition of total scattering cross section derived from the Mott-Massey [23] formulation. Reasonable agreement with data obtained earlier was found using the differential cross section formula for combined elastic and inelastic scattering defined by [24]:

$$\frac{d\sigma}{d\Omega} = 4\frac{\alpha^2 h^2}{p^2 \theta_\mu^4}\left\{1 + \frac{\theta_\mu^4}{Z}\left[\left(1 + \frac{\theta^2}{\theta_\mu^2}\right)^2 - 1\right]\right\}\left(1 + \frac{\theta^2}{\theta_\mu^2}\right)^{-2} \tag{24}$$

where θ is the scattering angle, α is the "Born parameter", $Ze^2/h\,v_0$, Z the atomic number of the target gas, v_0 is the electron velocity and θ_μ is the "Born screening angle", $1.12\ h/r_0 p$ and r_0 is the Thomas-Fermi radius, $0.885 h^2 Z^{-1/3} / m_e e^2$. If the Thomas-Fermi radius is multiplied by 2, as suggested by Lenz[28], both the Lee-Cooper model and the single scattering model described below exhibit satisfactory agreement with data.

The minimum angle of integration (in radians) relative to the beam axis, θ_{min}, with respect to which the integrations in (23) are performed to find solid angle, is taken to be:

$$\theta_{min} = I/4\ E \tag{25}$$

where I ($\approx$12.5 Z) = the mean ionization energy and E is the beam energy.

3.2 Single Scattering Approximation of Beam Electron Distribution.

With the assumptions that beam electrons are scattered via elastic and inelastic collisions with the gas molecules, that no electron suffers more than a single collision, and that the scattered electrons retain their initial energy, an approximate estimate of the distribution of electrons contained within an axisymmetric, non-relativistic electron beam can be calculated. It is also commonly assumed that electron scattering is well approximated by regarding molecules as separate spherical atoms.

The flux of singly-scattered electrons from an arbitrary control volume r' dv dr' dz, located at a radius r' and axial position ζ, passing through the area element, r' dϕ dr', located at z > ζ along the beam and with a surface normal parallel to the beam axis, is given by:

$$d\phi = [(r'\, dv\, dr')(n_0\, v_0)]\left(n_g \frac{d\sigma}{d\Omega}\right) d\omega\, d\zeta \tag{26}$$

where (r' dn dr') (n_0 v_0) is the flux of unscattered electrons through the control volume and (n_g dσ/dΩ) dω dζ is the probability of an electron being scattered from the control volume though the solid angle

$$d\omega = \frac{r\, d\phi\, dr \cos\theta}{\left[(z-\zeta)^2 + (\bar{r}-\bar{r}')^2\right]} \tag{27}$$

The differential cross-section dσ/dΩ is the same as used above, namely equation (24).

Integration of eq. (26) over the beam cross-section gives the flux through the area segment due to scattering at the position ζ along the beam. Subsequent integration with respect to ζ yields the flux from all positions along the beam. Dividing the flux by the segment area gives the scattered electron flux density. The number density of scattered electrons $n_1(r,z)$ is then just the flux density divided by the mean electron velocity:

$$n_1(r,z) = 2\int_0^z\int_0^r\int_{-\pi/2}^{\pi/2} n_g(\zeta)\, n_0(r',\zeta) \frac{d\sigma}{d\Omega}\, r'\, \Delta z \left(\Delta z^2 + \Delta r^2\right)^{-3/2} dv\, dr'\, d\zeta \tag{28}$$

where $\Delta z = z - \zeta$ and $\Delta r = | \bar{r} - \bar{r}' |$.

In the single scattering model, the total beam electron number density is assumed to be approximately equal to the sum of the number density distribution of the unscattered electrons $n_0(r,z)$ and singly scattered electrons $n_1(r,z)$. The root-mean-square beam radius, defined by (21), is calculated accordingly. The unscattered electron density distribution $n_0(r,z)$ is the initial density $n_0(r,z=0)$ multiplied by an exponential decay term representing the removal of electrons from the unscattered distribution due to scattering:

$$n_0(r,z) = n_0(r,0)\exp\left[-\int_0^z \beta d\zeta\right] \tag{29}$$

where b is the total scattering probability per unit length,

$$\beta(\zeta) = n_g(\zeta)\int_{\theta_{min}}^{\theta_{max}} \frac{d\sigma}{d\Omega}(2\pi\sin\theta)d\theta \tag{30}$$

The reference electron density distribution at z = 0, $n_0(r,0)$, provides the needed initial beam profile.

3.3 Multiple Scattering Approximation of Beam Electron Distribution.

The need for a multiple scattering beam electron distribution model arises because it is desirable to be able to use the e-beam fluorescence technique in relatively high density flows, such as those in the Mach 12 nozzle example. For the Mach 12 nozzle, a beam electron typically suffers 10's or 100's of collisions, casting significant doubt on the validity of the single-scattering approximation.

The model assumes that the electron angular distribution far from the gun aperture approaches a Gaussian form as the mean number of collisions per electron becomes large. This is essentially a consequence of the central limit theorem. Further, the model assumes that between the single-scattering and infinite scattering limits, the distribution is a weighted sum of the single-scattering and Gaussian distributions. Electron flux is assumed to be conserved over a hemispherical surface with a centroid at the point of entry of the beam into the gas flow.

The multiple-scattering electron beam model is intended to bridge the thin and dense approximations of beam propagation and to provide a more detailed electron distribution than the Lee-Cooper model and single-scattering models described in sections **3.2** and **3.3**. The multiple scattering model provides a more accurate distribution of the electron beam than either of the first two models for the range of gas number densities relevant to the Mach 12 nozzle hypersonic wind tunnel. In common with a the single-scattering calculation, the multiple-scattering model calculates the distribution of primary electrons as though they were scattered by spherical atoms, which is consistent with most analyses of electron scattering.

The need for a multiple scattering beam electron distribution model arises because it is desirable to use the e-beam fluorescence technique in the relatively high density flows to be found in wind tunnels. For a Mach 12 nozzle, a beam electron typically suffers 10's or 100's of collisions, limiting the validity of the single-scattering approximation. The Lee-Cooper model is a useful point of reference, but the assumptions upon which the model was derived are not valid once the beam has spread significantly. As well, the Lee-Cooper analysis assumes the distribution along the beam expands only radially and in a self similar manner.

The multiple-scattering code described here predicts the primary beam's divergence and the detailed electron beam distribution. The distribution is needed to predict accurately the spread of the beam due to anticipated multiple scattering of beam electrons and to estimate the flow volume that needs to be imaged in order to obtain useful information from fluorescence. As well, integration of the distribution coupled with a modified version of the photometric analysis described in Section **1.0** in turn enables prediction of the optically-measurable, spatially-varying fluorescence signal distribution due to primary excitation of species. This modified photometric analysis is described below in section **7.4**.

The model differs from earlier multiple-scattering analyses, most notably that given by Jacob[15], in that the angular distribution of beam electrons is of interest not at points remote from the target, where the beam diameter within the target can for the purpose of measuring scattering angles be assumed to be ignoble small. This is not the case here, since the angular distribution of electrons within the target itself is of main interest rather than the distribution after electrons emerge from the target.

Specifically, the model assumes that the electron angular distribution far from the gun aperture approaches a Gaussian form as the mean number of collisions per electron becomes large. This is essentially a consequence of the central limit theorem. Further, the model assumes that between the single-scattering and infinite scattering limits, the distribution is a weighted sum of the single-scattering and Gaussian distributions. Electron flux is assumed to be conserved over a hemispherical surface with a centroid at the point of entry of the beam into the gas flow.

The singly-scattered component of the electron flux is now attenuated, and is calculated on a sphere, rather than on a radial disk. The infinitesimal scattering volumes themselves, however, remain as angular segments of concentric annuli. The expression analogous to (26), representing the flux of singly-scattered electrons from an arbitrary control volume r' dν dr' dz', located at a radius r' and axial position z', passing through the hemispherical area patch, $l^2 \sin\theta \, d\theta \, df$, located on the surface of a sphere of radius l, centered at the beam entry point, and angle θ relative to the beam axis, is modified only by the attenuation factor, A:

$$\Delta\Phi = A(\nu, \nu', r, r', z, z')[(r' \, d\nu \, dr')(n_0 v_0)]\left(n_g \frac{d\sigma}{d\Omega}\right) d\omega \, dz' \tag{31}$$

where:

$$A(\nu, \nu', r, r', z, z') = \exp\left(-\int_{s_{cv}}^{s_p} \beta(s) ds\right) \tag{32}$$

and

$$\beta(s) = n_g(z' + s\cos\theta_s) \int_{\theta_{min}}^{\theta_{max}} \frac{d\sigma}{d\Omega}(2\pi \sin\theta) d\theta \tag{33}$$

(Note that the similarity between this expression for β and (30) above.) It is assumed here that the gas atomic number density, n_g, varies only in the z direction. Hence, along the straight line path, parameterized by s, between the control volume, denoted by s_{cv}, and the patch, denoted by s_p, the gas density varies as $s \cos\theta_s$, where θ_s is the scattering angle, found from:

$$\sin\theta_s = \frac{1}{l}\left[(r' \cos\nu)^2 + (l\sin\theta - r' \sin\nu)^2\right]^{1/2} \tag{34}$$

As before, (r' dv dr') (n_0 v_0) is the flux of unscattered electrons through the control volume and (n_g $d\sigma/d\Omega$) $d\omega$ dz' is the probability of an electron being scattered from the control volume though the solid angle, $d\omega$. Now, however, dw, defined as

$$d\omega = \frac{\text{(patch area)*(patch orientation relative to control volume)}}{\text{(distance from control volume to patch)}^2}$$

becomes:

$$d\omega = \frac{\left(l^2 \sin\theta d\theta d\phi\right)\left(\Delta\mathbf{p}\cdot\mathbf{n}/|\Delta\mathbf{p}|\right)}{|\Delta\mathbf{p}|^2} \tag{35}$$

where $\Delta\mathbf{p}$ is the vector from the control volume to the patch, $\mathbf{n}$ = (0, sin θ, cos θ) is the patch surface normal, and $\Delta\mathbf{p}\cdot\mathbf{n}/|\Delta\mathbf{p}|$ is the patch form factor. From **Figures 14(a)** and **(b)**, it is seen that

$$\Delta\mathbf{p} = \left(-r'\cos\nu, l\sin\theta - r'\sin\nu, l\cos\theta - z'\right) \tag{36}$$

where the control volume is at

$$\mathbf{p}_{cv} = \left(r'\cos\nu, r'\sin\nu, z'\right) \tag{37}$$

Therefore,

$$\Delta\mathbf{p}\cdot\mathbf{n} = l - r'\sin\theta\sin\nu - z'\cos\theta \tag{38}$$

and

$$|\Delta\mathbf{p}| = [r'^2 - 2r'l\sin\nu\sin\theta + l^2 - 2lz'\cos\theta + z'^2]^{1/2} \tag{39}$$

Hence,

$$d\omega = |\Delta\mathbf{p}|^{-3} l^2 \sin\theta\left(l - r'\sin\theta\sin\nu - z'\cos\theta\right)d\theta d\phi \tag{40}$$

The resulting flux density of singly-scattered electrons at θ is then the integral over all control volumes contributing to the flux at θ divided by the patch area:

$$F_1(\theta,l) = \frac{\left(\int_0^{z_c}\int_0^{r_0}\int_0^{2\pi} \Delta\Phi \, dn dr' \, dz'\right)}{l^2 \sin\theta \, d\theta \, d\phi} \tag{41}$$

or

$$F_1(\theta,l) = \int_0^{z_c}\int_0^{r_0}\int_0^{2\pi} A\, n_0 v_0 n_g \frac{d\sigma}{d\Omega} r' |\Delta\mathbf{p}|^{-3} (l - r' \sin\theta \sin v - z' \cos\theta) dv dr' dz' \tag{42}$$

For computational efficiency, variables in the integrand that can be evaluated outside of the inner integral are, of course. The upper bound on the r' integration, r_0 , is the radius of the beam of unscattered electrons. z_c is the cutoff point beyond which no significant scattering occurs from points within the beam through the patch. The definition of z_c is somewhat arbitrary, but is simply related to the (equally arbitrary) maximum single-scattering angle.

The number density of singly-scattered electrons from the control volume that pass through the patch at θ is

$$\Delta n_1 = \Delta\Phi / (\text{patch area})(v_0 \cos\theta') \tag{43}$$

where

$$\cos\theta' = \Delta\mathbf{p} \cdot \mathbf{n} / |\Delta\mathbf{p}|$$

This gives finally,

$$n_1(\theta,l) = \int_0^{z_c}\int_0^{r_0}\int_0^{2\pi} A\, n_0 n_g \frac{d\sigma}{d\Omega} r' |\Delta\mathbf{p}|^{-2} dv dr' dz' \tag{44}$$

In both (42) and (44), $d\sigma/d\Omega$ is calculated using the scattering angle, θ_s, in (34).

To conserve electric current, we wish to integrate electron fluxes over a hemispherical surface. The total flux of singly-scattered electrons is:

$$N_1(l) = 2\pi l^2 \int_0^{\theta_{max}} F_1 \sin\theta d\theta \tag{45}$$

The total flux of unscattered electrons is:

$$N_0(l) = (I/e)\exp\left(-\int_0^l \beta dz'\right) \tag{46}$$

where I is the beam current. Conservation of the total electron flux, N_t, over a hemisphere of radius l requires that;

$$N_t \equiv (I/e) = N_0(l) + N_1(l) + N_m(l) \tag{47}$$

where N_m is the multiply-scattered electron flux.

The angular distribution of multiply-scattered electrons is assumed to be approximately Gaussian, with a mean square angle of about:

$$\langle \theta^{*2} \rangle = s \langle \theta_s^2 \rangle \tag{48}$$

where s is the "target thickness", i.e. the integral expression in (46), and

$$\langle \theta_s^2 \rangle = \frac{\int_{\theta_{min}}^{\theta_{max}} \theta^2 \frac{d\sigma}{d\Omega} d\Omega}{\int_{\theta_{min}}^{\theta_{max}} \frac{d\sigma}{d\Omega} d\Omega} \tag{49}$$

which is the same mean square single-scattering angle as used for the Lee-Cooper model.

The accuracy of the foregoing assumption of a Gaussian distribution depends on the value of $s\langle \theta_s^2 \rangle$. For ease of analysis, let

$$P(\theta^*) = \theta^* - \frac{1}{6}\theta^{*3} + \frac{1}{120}\theta^{*5} - \frac{1}{5040}\theta^{*7} \tag{50}$$

serve to approximate sin θ^*. (Any approximation of this or higher order will suffice, since the accuracy of the Gaussian assumption is insensitive to approximation order above 7 when $s\langle \theta_s^2 \rangle >$ 1, which is of no interest.) Then

$$\langle\theta^{*2}\rangle \equiv \frac{\int_0^\infty \theta^{*2}\exp\left(-\theta^{*2}/c^2\right)(2\pi\sin\theta^*)d\theta^*}{\int_0^\infty \exp\left(-\theta^{*2}/c^2\right)(2\pi\sin\theta^*)d\theta^*}$$

$$\cong \frac{\int_0^\infty \theta^{*2}\exp\left(-\theta^{*2}/c^2\right)P(\theta^*)d\theta^*}{\int_0^\infty \exp\left(-\theta^{*2}/c^2\right)P(\theta^*)d\theta^*} \qquad (51)$$

$$= c^2\frac{1-\frac{1}{3}c^2+\frac{1}{20}c^4-\frac{1}{210}c^6}{1-\frac{1}{6}c^2+\frac{1}{60}c^4-\frac{1}{840}c^6}$$

where

$$c^2 \equiv s\langle\theta_s^2\rangle \qquad (52)$$

and

$$f_m(q^*,l) = K(l)\exp\left(-\theta^{*2}/c^2\right) \qquad (53)$$

is the assumed angular distribution of multiple scattering. (53) is of the same form as Fermi calculated [33], with s replaced by s/3, and has been shown to give satisfactory agreement in the large multiple-scattering limit [8]. Thus, Fermi's result is used in the current implementation.

As $c \to 0$, $\langle\theta^{*2}\rangle \to c^2$. However, even as high as $c = 1$, $\langle\theta^{*2}\rangle$ differs from c^2 by less than 16%, regardless of the approximation order for $\sin\theta$. With (53) as the definition of the multiple scattering distribution, the total hemispherical flux of multiply-scattered electrons is:

$$N_m \equiv 2\pi K(l)\int_0^{\pi/2}\exp\left(-\theta^2/c^2\right)(\sin\theta)d\theta$$

$$\cong 2\pi K(l)\int_0^{\pi/2}\exp\left(-\theta^2/c^2\right)P(\theta)d\theta \qquad (54)$$

$$= \pi K(l)c^2\left(1-\frac{1}{6}c^2+\frac{1}{60}c^4-\frac{1}{840}c^6\right)$$

where the difference in upper integration bound affects the result at most by 5% in the limit that c $\rightarrow$1. Accuracy improves as c $\rightarrow$ 0.

The constraint, (47), now yields K(l) from (54). Consequently, the multiply-scattered electron number density is

$$n_m(\theta, l) = \frac{1}{v_0 l^2} f_m(\theta, 1) = \frac{K(1)}{v_0 l^2} \exp\left(-\theta^2/c^2\right) \tag{55}$$

which follows from comparison of the total electron fluxes through an angular range dθ at angle θ on the sphere of radius l :

$$n_m v_0 (2\pi r) l d\theta = f_m (2\pi \sin\theta) d\theta \tag{56}$$

where $r = l \sin\theta$.

For comparisons with our earlier results and with published data and theory, total number densities of scattered and unscattered electrons are calculated at positions on spheres (l, θ) and on radial disks (r, z). So

$$n_t = n_0 + n_1 + n_m \tag{57}$$

for either calculation.

3.4 Modification of Scattering Cross Sections.

Center [8] has reported satisfactory agreement between Monte Carlo calculations and experimental data over a non-relativistic beam energy range, 20-100 keV, using a cross-section formula that does not explicitly depend on $\beta = v_0/c$. One of the parameters Center used in the formula was derived from comparison with an earlier report [27] on scattering measurements of 615 keV electrons in N_2, suggesting that relativistic electron beam spread may also be reasonably well modeled with this cross section.

Center's formulae [8] for the combined elastic and inelastic scattering cross sections has the form:

$$\frac{d\sigma}{d\Omega} = \sigma_R(\theta)\left\{\left[1-F(\theta)\right]^2 + G(\theta)/Z\right\} \tag{58}$$

where σ_R is the Rutherford cross section, which ignores screening,

$$\sigma_R = \frac{Z^2 e^4}{4 p^2 v^2 \sin^4 \theta/2}. \tag{59}$$

Here, e, p, and v are the electron charge, momentum and velocity, respectively. θ is the scattering angle. In (58) $F(\theta)$ is the "screening factor", or "atomic form factor":

$$1 - F(\theta) = K(\theta)\sum_{i=1}^{3}\frac{a_i}{\left(Z^{1/3}b_i/121\right)^2 + K(\theta)} \tag{60}$$

where

$$K(\theta) = \left(\frac{2\lambda_0}{\lambda}\sin\frac{\theta}{2}\right)^2 \tag{61}$$

λ_0 is the Compton wavelength, λ is the de Broglie wavelength, and a_1=0.10, a_2=0.55, a_1=0.35, b_1=6.0, b_2=1.2, b_3=0.3. $G(\theta)$ represents the component of the cross-section due to inelastic scattering, as obtained by Lenz[28] for exponential screening:

$$G(\theta) = 1 - \left[1+\left(\frac{2\pi\theta}{\lambda}\right)^2 a_s^2\right]^{-2}. \tag{62}$$

In (5), a_s is the "screening parameter", which Center assumed to be 3.7×10^{-9} cm for Nitrogen based on the above cited report [27]. Consistent with equation (25), the validity of (62) is generally assumed to be limited to:

$$\theta \geq I/4E \tag{63}$$

where I is the mean ionization energy, (about 12.5 Z), and E is the beam energy. Expression (60) for elastic scattering, derived from the Moliere potential, is normally used at moderate to large scattering angles. Center's criterion was that

$$\frac{2\lambda_0}{\lambda}\sin\frac{\theta}{2} \geq 0.07 \qquad (64)$$

For small angle scattering, Hartree screening [30] has been found to better approximate elastic scattering, and values of $F(\theta)$ have been tabulated by Ibers [29]. Unfortunately, this tabulation was not available for the current report. In any event, the inelastic cross-section dominates small angle scattering, so that the error resulting from using (60) is generally less than 10%. (60) over estimates elastic scattering by about a factor of 6 or 7 near $\theta = 0$, for the 100 keV beam in N_2.

In **Figures 15 (a)**, **(b)** and **(c)**, elastic, inelastic and combined elastic and inelastic scattering cross sections based on the above formulae are compared for each of three energies: **(a)** 20 keV, **(b)** 50 keV and **(c)** 100 keV. **Figure 15(c)** essentially reproduces Center's Figure (1), except for the error in the elastic cross-section just cited, and the choice of abcissa scaling--we used θ, Center used $K^{1/2}(\theta)$. The inelastic cross-section is the same. The cross-over point between the elastic versus inelastic dominated scattering cross-section corresponds approximately to the threshold just cited, equation (64).

Several trends may be noted from **Figures 15(a)**, **(b)** and **(c)**. First is that the cross-sections generally decrease with increasing energy, as expected, though more slowly at higher beam energies. Second is that at lower beam energies, inelastic scattering tends to dominate elastic over a larger angular range, implying comparatively faster rate of beam energy loss along the beam axis. Finally, it may be noted that the elastic scattering cross-section decreases more slowly than the inelastic with increasing beam energy, at least at small angles.

4.0 Spatial and Spectral Distribution of Electron Beam Fluorescence

4.1 Beam Divergence Predictions from Envelope and Single Scattering Models

Based on comparisons made so far [26] with fluorescence data at low gas densities, the single-scattering model is in good agreement with the experimental measurements and indeed more closely predicts beam spread than does the multiple-scattering envelope model. In addition, the single-scattering model is better suited for use in predicting beam spread in a variable-density medium such as a hypersonic nozzle or shock layer where the gas density will vary as a function of distance along the beam path. The dependence of gas density on z, $n_g(z)$, is implicit in all of the above single scattering analysis, though not yet in the Lee-Cooper model.

For wind tunnel experiments, the choice of the electron-beam accelerating voltage will depend on both the spatial resolution and signal acquisition requirements. Since the scattering cross section for the electron beam decreases with increasing beam voltage, beam spread will be less rapid at higher operating voltages and thus spatial resolution will be improved. However, because the excitation cross section will also tend to be smaller, less total fluorescence signal would measured, implying a longer signal integration and loss of temporal resolution. In **Figure 13** a comparison of the calculated rms beam radius for 20, 50 and 100-keV electron beams from the multiple-scattering envelope model and single-scattering model are presented for three gas densities in a Mach 12 nozzle flow. The variation in beam spread with gas pressure is evidently much less significant over the narrow pressure range over which the nozzle is operated, than is the effect of beam energy. At all pressures, the multiple scattering model predicts such rapid spread, that low energy beams cannot penetrate the core flow, rendering the beam effectively useless for spatially resolved measurements. Also striking from these plots is the significant gap in predicted spread between the single- and multiple-scattering models. Thus there is a case for having pursued the previously described multiple-scattering distribution analysis in order to better model the dense nozzle flows.

4.2 Beam Divergence Predictions from Multiple-Scattering Electron Beam Model.

In **Figure 16(a)**, **(b)** and **(c)**, comparisons are made of the beam root-mean-square spread calculated from our current three models, viz. the Lee-Cooper model [17] described in section **3.1**, the single-scattering model, described in **3.2**, and the multiple scattering model, described in **3.3**. In the current calculation, the beam is assumed to traverse a Mach 12 hypersonic wind

tunnel nozzle. The models have all been modified to cope with non-uniform gas density distributions for this nozzle presented, as discussed in **1.0**. In this simulation, the following 7th order polynomial represents the number density distribution, based on a least squares fit of data shown in **Figure 6** at 1 cm intervals across the nozzle diameter:

$$f(z) = \sum_{j=0}^{7} q_j z^j, \quad 0 \le z \le 25.4\text{cm} \tag{65}$$

where q_0=7.3039×10^{16}, q_1=-1.8107×10^{15}, q_2=1.6443×10^{15}, q_3=-58923×10^{14}, q_4=8.5121×10^{13}, q_5=-5.7278×10^{12}, q_6=1.8012×10^{11}, q_7=-2.1498×10^{19}. This corresponds to a flow core density of fluctuating around 7×10^{16} per cm^3.

At 20 keV, **Figure 16(a)**, the single-scattering model apparently grossly underpredicts beam spread, which is merely consistent with intuition based on the estimated target thickness of 45 collisions per electron. The multiple scattering analysis suggests that the beam has expanded by about a factor of 30 by the time it reaches the core nozzle flow, rendering the beam useless for resolving flowfield fluctuations at the core edge less than about 3 cm, assuming the initial beam diameter is of order 1 mm. At the flow centerline the beam diameter is well over 10 cm, and the assumptions for which the model holds (no beam energy loss, small angle scattering) are violated. Beam electrons probably would not penetrate the flow, except due to electrostatic effects as thermalized free electrons accumulate in the flow or are convected downstream.

At 50 keV, **Figure 16(b)**, beam divergence is still very significant, though flow feature variations of order 2 cm or less at the flow centerline still cannot be resolved. At 100 keV, **Figure 16(c)**, the beam appears likely to yield useful information through most of the flow, and presumably simulations at higher energy would give correspondingly higher spatial resolution. However, above 100 keV, relativistic effects become significant enough that their inclusion becomes necessary for accurate divergence prediction.

4.3 Beam Profile Predictions from Multiple-Scattering Electron Beam Model.

Root mean square predictions are not the only useful measure of beam spread however. Since most commercial frame grabbers currently available are able to resolve grey levels in the range of 2^8-2^{12}, corresponding to a dynamic range of from 256 to 4096 or 2.4 to 3.6 orders of magnitude, it is necessary to evaluate the radial distribution of primary electrons, whose number

density distribution corresponds to the expected fluorescence distribution, in order to determine the spatial region over which fluorescence can be integrated computationally from a digital image.

Thus in **Figures 17(a)**, **(b)** and **(c)** we have plotted the expected number density distributions across the beam at two axial locations, viz. the flow centerline and the point of emergence of the beam from the flow core, using the multiple-scattering analysis. Again, **(a)**, **(b)** and **(c)** correspond to the three energies: 20 keV, 50 keV, and 100 keV. The initial beam is assumed to have a Gaussian form, in terms of the radial number density distribution. Beam electrons are initially unidirectional and mono-energetic. Since real beams do not generally consist of unidirectional electrons, and do suffer energy loss as a result of scattering, it is expected that the plotted distributions are optimistically narrow.

At 20 keV, **Figure 17(a)**, the profile is predominantly Gaussian, and a broad distribution tail has formed. Since an 8-bit frame grabber would be able to resolve a 2.4 decade range, the figure suggests that fluorescence at the flow centerline, 25.4 cm, covering about a 12.5 cm radius could probably be measured, though resolution of flow features would no doubt require flow imaging from multiple angles combined with significant computational tomographic reconstruction. This is not normally how e-beams are used as flow diagnostics, and it is far from clear that fluorescence due to a such widely dispersed beam would have a straightforward quantitative interpretation.

At 50 keV, **Figure 17(b)**, there is still a significant concentration of electrons within a 2 mm radius from the beam centerline at flow centerline. The broad shallow tail of the distribution corresponds to large angle singly-scattered electrons, the sharp peak near the beam centerline consists predominantly of multiply-scattered electrons, whose angular dispersion is relatively narrow until beam electrons have suffered a large number of collisions on average. The large values of r.m.s. radius seen in **Figure 16(b)** at this position suffer from a significant bias due to the radius-squared weighting of such a broad tail, tending to confirm the need for a distribution analysis as a beam prediction tool. At 50.4 cm, where the beam emerges from the flow, it is evident that the beam has rapidly degraded.

At 100 keV, **Figure 17(c)**, the expected distribution shows that beam electrons over a three decade density range are confined to within about a 5 mm radius. Thus fluorescence outside this radius would not be detected upon image digitization.

4.4 Development of a Model for the Measurement of Nitrogen Density and Rotational Temperature Using Band Pass Filters.

In EBF studies and others, the preceding theoretical analysis in section **2.1** is used to determine the rotational temperature of a gas from experimental rotational spectra. However, to correctly use the theory on experimental data requires that the rotational "lines" of the experimental spectra be independent of each other. Of course, no actual spectra consist of pure lines, but have finite line shapes. The line shapes arise from broadening mechanisms such as: natural line broadening due to the finite lifetimes of the transition, Doppler broadening resulting from the translational motion of the molecules, pressure broadening, and the broadening due to the bandwidth of the optical equipment being used. Generally, natural line broadening has the smallest effect, while pressure and Doppler broadening effects may be reduced or removed, depending upon the nature of the experiment. Broadening due to bandwidth of the spectral instrument used for measurement, however, is generally dominate and dependent on the resolution of the instrument. All of these effects can combine to such a degree that in the resulting experimental spectra obtained, what were theoretically rotational lines have now become line shapes, that can overlapping each other in part or all of the spectra. This results in the observed intensities deviating from the theoretical model for the spectrum and modifications to the theory must be made to account for the overlapping spectrum.

Typically, high resolution spectra are obtained using a spectrometer with a diffraction grating. The diffraction grating diffracts the incoming light with enough resolution such that the lines of the wanted rotational spectra are adequately separated. Higher resolution can be attained simply by changing diffraction gratings to one with more grooves per millimeter. In addition, the spectrometer entrance slit width can also be varied which directly affects line broadening and image intensity. The slit width can be reduced, thereby increasing the resolution. However, this also reduces the signal intensity. Also, critical alignment of the optical instruments of the experiment is needed for a high quality signal. This alignment process may be very delicate and need a very stable platform to assure that the spectrometer is acquiring the optimal image. Thus although high resolution is commonly possible using a spectrometer, the method can require much effort and ideal conditions to operate effectively. This may cause difficulties in some situations, such as aboard an aircraft or in wind tunnel application.

A more direct approach to acquiring rotational spectra data is not to diffract the light containing the rotational transition information but to use bandpass filters to acquire the rotational

intensities. A discussion of bandpass filters is presented in sections **5.1** and **6.1** of this report. Using filters, a spectrometer with a diffraction grating is no longer needed. This saves in equipment costs. Also, the line broadening and required adjustments associated with the spectrometer slit width are removed. Similarly, the experiment would not be as easily disturbed since fewer optics would be required and therefore more easily aligned and maintained. In this way, one or several filters could be used to effectively select different wavelengths and their associated intensities through the use of a photomultiplier and again determine the rotational temperature.

One of the objectives of this study was to determine techniques for the measurement of the rotational temperature of a gas. As previously discussed, one method to do this would be to use a spectrograph to obtain the entire rotational spectra and then utilize the theory of section **2.1** to obtain the rotational temperature. However, since the intensity of an emission depends on rotational temperature, if it were known how a particular rotational line's intensity varied with temperature then it should be possible to simply note the observed intensity of a particular line and thereby obtain the rotational temperature. Unfortunately, this also requires a one-to-one correspondence between line intensity and temperature.

As shown in **Figure 8**, there is not necessarily a one-to-one correspondence. In particular, the low rotational quantum number line intensities increase and then decrease with temperature. Further, if intensity varies slowly with temperature then it is more difficult to obtain an accurate temperature reading since a relatively large change in temperature would cause a relatively small change in intensity, and therefore an observer would not be able to notice this large difference in temperature. Also, it is not feasible to only observe rotational lines because filters transmit certain wavelengths of light, not particular rotational lines. Thus, different rotational line intensities will move through a filter's window as temperature changes. In addition, the filter has a finite bandwidth and therefore the observed intensity may have contributions from not just one rotational line, but possibly several. This is similar to the overlapping effect inherent with spectrometer discussed earlier, but it will not cause serious difficulties with this method.

Note in **Figure 8** for K' = 5 that there is a steep rise in intensity at low temperatures (T_r <10 K), but then intensity slowly decreases. This would be a good line to observe only for very low temperatures. The K' = 20 curve is good from about 150 K to 400 K after which the curve flattens out. The K' = 40 curve does not even attain 0.001 relative intensity until about 600 K, but is a reliable function of temperature up to an slightly beyond 1000 K. Thus, it seems that

several lines in combination should be utilized to satisfactorily ascertain temperatures from the very low regime up to 1000 K. However, as noted before, filters transmit certain wavelengths, not quantum numbers, and these filters also have a bandwidth and shape.

5.0 Optical Filtering Schemes for Gas Density and Temperature Measurements

5.1 Design of Bandpass Filters for Imaging of Electron Beam Fluorescence in Nitrogen.

In this section recommendations are presented on the design of band-pass filters for imaging of the fluorescence from nitrogen for density and rotational temperature measurements. Although there are several different types of bandpass filters, interference filters are the most appropriate for observing rotational spectra because they can achieve smaller bandwidths than simple colored glass filters while still maintaining relatively high transmittance.

Interference filters utilize the phenomenon of interference to transmit or reflect certain spectral regions. They are made by combining thin, accurately parallel, transparent dielectric slices coated with reflective layers applied to each surface. When two of these dielectric slices are separated by and attached to an optically thick material of the proper thickness, the result is a Fabry-Perot etalon, or more commonly, a *cavity*. The reflectance and interference through these cavities causes the transmittance of only certain wavelengths of incident light. Typically, one, two or three of these cavities are combined to produce the desired filter shape. Also, other types of filters with high transmittance can be combined to block unwanted harmonics. In the nitrogen first-negative system, the significant unwanted harmonics occur at 427.8, 470.9, and 358.2 nm.

The spectral region of interest in the nitrogen first-negative band is between approximately 384 to 391 nm. This is a difficult area to build efficient filters at small bandwidths. The smallest bandwidth reasonably possible has been determined to be 2.2 ±0.5 nm with a corresponding peak transmittance of 50 % utilizing a two cavity interference filter. The lines of the P-branch should be blocked as much as possible by the filter since these lines will not be used to determine rotational temperature and thus will only cause unwanted interference effects. Therefore, the filter must block wavelengths from 391 nm to 392 nm to minimize P-branch interference although at high temperatures ($T \cong 500\ K$), P-branch lines begin to overlap the R-branch which is unavoidable and beyond the blocking effect of the filter.

There are two ways of using interference filters applicable to observing rotational spectra. Either several filters can be made at varying nominal wavelengths (e.g. separate filters at 384 nm, 386 nm, etc.), or a single filter can be tuned to a particular wavelength. This tuning of nominal wavelength is obtained by changing the angle of incidence of the filter relative to the incoming

beam of light. The nominal wavelength is shifted to a lower wavelength due to the increased apparent distance the light has to travel through the different elements of the filter according to the following equation,

$$\lambda_\theta = \lambda_0\{1-(n_0/n^*)\sin^2\theta\}^{1/2} \qquad (66)$$

where λ_θ is the shifted nominal wavelength, λ_0 is the designed nominal wavelength ($\theta = 0$), n_0 is the refractive index of the medium surrounding the filter (e.g. air), and n^* is the effective refractive index of the filter. The transmittance is not significantly reduced as a result of changing the angle of incidence.

The optimal filter design applicable to fluorescence imaging from nitrogen is a two-cavity interference filter. Its half-peak bandwidth can be as low as 2.2 ± 0.5 nm with a peak transmittance of 50 %, and unwanted wavelengths have been blocked. The effective refractive index n^* is 1.38. If it is desired to tune a single filter for certain wavelengths, it is advised to use a filter with a nominal wavelength of 392 nm. With this design, 384 nm can be tuned with a 11° angle of incidence and only a 10 % loss in peak transmittance.

A commercial filter design was obtained from CVI Laser, Inc. and a filter shape was also obtained. This filter shape was then approximated with a Gaussian curve-fit to be used in a FORTRAN program which outputs the predicted intensity seen by the filter as a function of temperature at a particular wavelength of the rotational spectra. The program computes this predicted intensity by first picking a wavelength to be set as the nominal position of the filter. Then a loop is started to vary rotational temperature from 5 K to 1000 K in increments of 5 K. At each temperature, the theoretical rotational spectra is computed via the analysis of reported in section 1 of this report. The program then looks for rotational lines near the prescribed nominal wavelength within the limits of the filter. Any lines within the filter window are then multiplied by their corresponding transmittance through the filter using the Gaussian function approximating the filter shape, and these scaled intensities within the filter window are then added together and finally sent to an output file along with the corresponding temperature. The temperature is then raised by 5 K and the process repeats until 1000 K thus creating data for intensity versus temperature for a given nominal wavelength and given filter shape.

This program was run for nominal wavelengths of 384, 385, 386, 387, 388, 389, 390, and 391 nm with half-peak bandwidths of 0.1, 1.0, and 3.0 nm. The resulting graphs of this data are

shown in **Figure 9(a)-(c)**. Although CVI Laser, and other optical companies, can only produce interference filters in this wavelength range with bandwidths as low as 2.2 ± 0.5 nm, while maintaining reasonable transmittance, a 0.1 nm bandwidth was included in this study to ascertain whether advances in optical technology would significantly benefit the filter method of obtaining rotational temperature. As seen in **Figure 9(a)**, a 0.1 nm bandwidth produces mixed results. A nominal wavelength of 390 nm is good for low temperature measurements (≤ 150 K), but this curve then flattens out, and then another wavelength should be looked at for higher temperatures. The 1.0 nm bandwidth graph of **Figure 9(b)** has better results since a larger temperature range is possible with all the wavelengths, except at 390 and 391 nm where the curve is consistently flat. In **Figure 9(c)** may have the best results, where the 386 nm wavelength's intensity can be used to obtain rotational temperatures from the very low regime up to the mid-200 K range and the 384 nm can be used from where the 386 leaves off all the way to 1000 K. Therefore, using a very small bandwidth such as 0.1 nm does not improve temperature measurements, but in fact the current technology in filter optics is adequate to determine rotational temperature. In all of this analysis, it is assumed that the photomultiplier being used has the capability of resolving intensity measurements as low as 0.1 % of maximum.

It is therefore recommended that an interference filter in the 2-nm to 3-nm range be used to observe intensities at wavelengths from 384 to 386 nm to determine rotational temperatures. Again, this may be done by tuning one filter to the appropriate wavelength, or using several static filters specifically designed for certain wavelengths.

6.0 Design Characteristics of an Improved Fluorescence Imaging System

6.1 Selection of Reference Filter for E-Beam Fluorescence Density and Temperature Measurement.

In the preceding discussion in section **5.1** it was recommended that band pass filters be used, rather than a spectroscope, to measure the fluorescence signals to calculate rotational temperatures. This is particularly necessary for imaging applications. Using a filter with a specified bandwidth and center wavelength and a theoretical model of a rotational transition emission, the intensity transmitted through a filter can be calculated as a function of rotational temperature. An example of the result is shown in **Figure 9(d)** at several different center wavelengths. Thus, it is possible to determine the rotational temperature by recording the intensity through a given filter, referring back to the theoretical intensities and determine the rotational temperature corresponding to the measured intensity. A limitation of this method is that a reference intensity must be identified to correlate the measured intensities to the theoretical model. This problem can be eliminated if ratios of intensities from two filters with different center wavelengths are used. This ratio is now non-dimensional and therefore theory and experiment are normalized.

Referring to **Figure 9(d)** a nominal wavelength of 2.0 nm was used to produce this analysis. This bandwidth was chosen since it is currently the smallest practical bandwidth possible without severe penalties in transmission and cost. Also, as can be seen from **Figure 9(d)**, smooth curves result from this bandwidth. Therefore, 2.0 nm will be used as the bandwidth throughout this study.

At a center wavelength of 390 nm, a filter used to observe the electron beam fluorescence in the (0,0) band of produces a flat curve or relative high intensity over the entire range of temperature. This insensitivity in signal level as a function of temperature makes the 390-nm unsuitable for determining the rotational temperature, but does make it very desirable as a reference intensity or for use in the measurement of density. Therefore, the intensity measured from the 390 nm center wavelength filter will be used as the reference intensity,.

$$I^*(T) = \frac{I(T)}{I_{ref}(T)} = \frac{I(T)}{I_{390nm}(T)} \tag{67}$$

where $I^*(T)$ is the non-dimensional intensity as a function of temperature. A plot of I^* for various center wavelength filters versus temperature is presented in **Figure 10**. The results are similar to that in **Figure 9(d)**, but the vertical axis is on a scale normalized by the intensity from the 390 nm filter.

6.2 Temperature Measurement Accuracy and Required Signal Acquisition Time.

To achieve high accuracy in determining a rotational temperature a filter ratio should be chosen that gives a large variation in signal with temperature. Relatively good sensitivity for the 387-nm filter is obtained for temperatures below about 600 K. With this curve, as temperature changes there is a significant change in measured intensity. Therefore, the 387 nm curve is a good choice for measuring temperatures below 600 K. To place the selection of filter ratios on a rigorous basis an analysis of signal uncertainty is presented :

We define the precision or uncertainty in the non-dimensional filter signal ratio to be

$$\frac{\Delta I^*}{I^*}(T) = \sqrt{\left(\frac{\Delta I(T)}{I(T)}\right)^2 + \left(\frac{\Delta I_{ref}(T)}{I_{ref}(T)}\right)^2} = \sqrt{\left(\frac{\Delta I(T)}{I(T)}\right)^2 + \left(\frac{\Delta I_{390nm}(T)}{I_{390nm}(T)}\right)^2} \qquad (68)$$

The slope of $I^*(T)$ is defined as $\frac{\Delta I^*}{\Delta T}$, which can be calculated by finite differences. Therefore, the uncertainty in a temperature measurement, as a function of the temperature, is given by:

$$\frac{\Delta T}{T}(T) = \frac{\Delta I^*}{I^*}(T) \times \frac{I^*(T)}{\frac{\Delta I^*}{\Delta T}(T)} \times \frac{1}{T} \qquad (69)$$

Thus, for optimal accuracy there should be a low filter signal ratio uncertainty, $\frac{\Delta I^*}{I^*}$, and a large slope, $\frac{\Delta I^*}{\Delta T}$. However, other factors involved in accurate temperature measurement must be considered.

A limitation of the filter-ratio method is that there is a minimum intensity which can be reasonably observed with a measuring device, such as a photomultiplier. It is assumed throughout this study that an minimum intensity of 1 % of full-scale can be measured in a

reasonable signal acquisition time. We chose the intensity of the 390-nm filter as the maximum intensity level. Thus, if the 390 nm intensity is approximately 10 as shown in **Figure 9(d)**, then the minimum observable intensity would be 0.1, and as shown in **Figure 9(d)** this limits the temperature range possible for certain center wavelength filters. For example, the lowest temperature that a filter with a center wavelength of 387 nm could measure used to measure is 300 K. For the 386-nm filter the lowest possible temperature would be about 550 K. Another important factor in obtaining a sufficient accurate filter signal ratio is the time required to acquire the signal. We assume for analysis purposes that the minimum acceptable signal precision is ± 1% for the 390-nm filter. The time required to acquire this signal using the 390-nm filter is τ. This characteristic τ will be used as a reference time from comparisons with the signal acquisition time from other filters. By extending the acquisition time of the measuring device (i.e. photomultiplier tube or array detector), improved signal-to-noise ratios are achieved. For this analysis we assume that a sufficient signal acquisition time is maintained to produce a signal-to-noise ratio exists such that the uncertainty in filter ratio is less than or equal to 1%.

To attain this accuracy in filter ratio uncertainty, the exposure time required is inversely proportional to the filter ratio itself since τ is dependent on the 390 nm intensity, and the 390 nm intensity is also used to non-dimensionalize all intensities. Hence,

$$t^* = \frac{t}{\tau} = \frac{\text{exposure time required to attain } \dfrac{\Delta I^*}{I^*} \le 1\%}{\text{exposure time to acquire 390 nm intensity}} = \frac{I_{390nm}(T)}{I(T)} = \frac{1}{I^*(T)} \qquad (70)$$

where t^* is the non-dimensional time required to achieve an accuracy of one per cent in the intensity ratio. By calculating the uncertainty of any temperature measurement, as well as the non-dimensional time required to attain this accuracy, t^*, as a function of temperature, an assessment of the feasibility of obtaining rotational temperatures with specified filter ratios can be analyzed.

Using the equations above a FORTRAN program utilizing finite differences for all quantities (i.e. ΔT, ΔI^*,etc.), $\dfrac{\Delta T}{T}$ and t^* was developed. The results of the analysis of uncertainty for various filter ratios with this program are plotted as a function of temperature in **Figure 11**. The filter ratio for 388 nm is not generally recommended for use in temperature measurements since it has associated uncertainties of 10 to 25 % with a measurement precision of 1 % in the intensity ratio. For temperature measurements below 120 K as will be described below

the 388-nm filter can be used but with increased signal acquisition time to improve the precision in the intensity ratio. The other curves for filter ratios corresponding to 384, 385, 386, and 387 nm have excellent accuracies, however with varying required acquisition times as shown in **Figure 12**.

If rotational temperature measurements are desired for temperatures less than 300 K, from **Figure 11** the 387-nm filter is the only filter which can detect temperatures in this range. From **Figure 11** an uncertainty of 3% or better is possible. The relative signal acquisition time required to attain these accuracies varies between 500τ for 120 K temperature measurements to 40τ for 300 K temperature measurements, as shown in **Figure 12**.

If it is desired that the full temperature range is to be measured while maintaining the lowest possible uncertainties. From **Figure 11** the best accuracy is obtained by using four filters set to center wavelengths of 384, 385,386, 387 nm, and the reference filter at 390 nm. A maximum uncertainty of 3.5% results from the 387-nm filter while covering a range in temperature from 200K to 400 K. Similarly, the 386 nm filter would be used in the 400 K to 600 K measurements with a maximum uncertainty of 2.5%, the 385 nm filter for 600 K to 800 K with a maximum uncertainty of 2%, and the 384-nm filter for temperatures from 800 K to 1000K with a maximum uncertainty of 2%. The maximum time required to attain these temperature measurements would be 500τ. These results are summarized in Table II.

Table II. Summary of Filter Ratio Temperature Measurement Recommendations

Requirements	Filter Wavelengths*	Temperature Range
•Lowest possible uncertainties	387 nm	200 K - 400 K
	386 nm	400 K - 600 K
	385 nm	600 K - 800 K
	384 nm	800 K - 1000 K

7.0 Image Processing Schemes for Quantitative Flow Field Mapping

7.1 Image Processing and Data Visualization Considerations.

The procedure for modeling the primary electron distribution described previously calculates electron number densities along successive, concentric circular arcs, each centered at the point (z, r) = (0,0), defined as the point of entry of the electron beam into the gas at the beam centerline. Electron number densities are calculated at constant angular increments along each arc. At the plane at which the beam enters the gas, however, densities are calculated along off axis points at z=0 along a radial line normal to the beam axis.

Visualization of primary-excited fluorescence is desired in order to estimate the spatial extent over which a fluorescence imaging system could obtain useful data and to determine the probable photometric throughput achievable with a given system. For convenience, visualizations performed for this research were computed for a 640×480 rectangular format for display on VGA screens, and cropped to 640×480 for printing. While any format could be used including non-rectangular, a rectangular matrix, with row elements corresponding to positions parallel to the beam axis and column elements corresponding to radial positions, simplifies the projection of radially distributed data to a plane parallel to the beam axis. The need for projection of data is clear because an imaging system measures line-of-sight intensities through the beam, rather than volumetric fluorescence as a function of radius.

7.2 Interpolation Procedure for Determining Grey Scale Pixel Map.

Conversion of data from the polar format just described to a VGA-dimensioned matrix involves, first, transformation of pixel coordinates to physical Cartesian coordinates, z-r, which are axial-radial beam dimensions. The scaling chosen was simply that the 640 pixels in the horizontal dimension corresponds to 50.4 cm, the total length of the beam along a line crossing the flow. The number of pixels in the vertical direction, 480, correspond to a proportionately small distance, viz. 480/640×50.4 cm=37.8 cm. (The fact that pixels may not be perfectly square is of no significance at this stage. However, most display devices, such as computer screens have nearly a 4/3 aspect ratio, so the assumption of square pixels may not be too bad.)

Second, each pixel's physical Cartesian coordinates are transformed to polar coordinates, except near z=0, where the transformation is singular. Since fluorescence was evaluated at

regular angular intervals, the mesh of points in the simulation is rectangular in beam-axial-distance/angle (s-θ) space. Hence, fluorescence at the point of interest (the transformed pixel coordinate) can be found be any of several interpolation procedures. We chose bilinear interpolation for simplicity.

The region near z=0 requires a separate interpolation procedure. In this region fluorescence has been calculated at regular z-r positions, which obviates the need for transforming pixel coordinates to polar coordinates. Again bilinear interpolation is used. In the region where there is overlap between the rectangular and polar computational meshes, pixel values are found using the polar coordinate interpolation procedure.

7.3 Projection of the Radial Fluorescence Distribution.

Figure 18 illustrates the projection method to obtain side-view line-of-sight fluorescence distributions. The fluorescence emitted at each radial position corresponds to a radial "shell" around the beam center. A line of sight calculation involves simply multiplying the volumetric fluorescence at each shell by the area of the shell segment along a line of sight at a fixed off-axis position, r_i, and then adding the fluorescence contributions of each segment out to the beam radius. The radius was chosen to be sufficiently large to include all non-zero data obtained via the above described interpolation.

The inverse procedure, sometimes referred to as "onion-peeling" [21], determines the radial volumetric fluorescence from line-of-sight measurements. Abel inversion [19] is mathematically equivalent, but can be computationally more sensitive to measurement errors, depending on the emission distribution.

7.4 Local Photometric Analysis.

The model described above in section **1.0** for deriving photometric throughput can be modified for a beam with a non-uniform distribution of primary electrons by replacing equation (5) with a brightness function based on side-view observation of the line-of-sight fluorescence distribution. This expression is obtained by integrating the excitation rate, W_{00}, which is the product of electron number density, n_e, electron velocity, v_e, and the excitation cross-section, E_{00}, along the line of sight. The result is the brightness function:

$$B_\lambda = \left(\frac{A_{00}}{1/\tau_{rad} + Q_0} \right) \frac{E_{00} v_e n_g \int_{-y_0}^{y_0} n_e dy}{4\pi} \qquad (71)$$

where $y_0 = y_0(r) = \sqrt{r_0^2 - r^2}$, r_0 is the beam outer radius, and r is the off axis location of the line-of-sight. Note that if n_e were uniform within the beam the expression (5) would be recovered by integrating (71) with respect to r between the limits $-r_0$ and r_0 and dividing the result by $2r_0$. This is consistent with the concept of defining brightness as being proportional to the source volume divided by the source projected area and by 4π steradians. For the electron excited optical-emission cross section for the (0,0) band of the N_2^+ first negative system we have used the standard form of the non-relativistic expression [23,31]:

$$E_{00} = (A/E) \ln (BE) \qquad (72)$$

where, according to Lewis [32], $A = 1.69 \times 10^{-15}$ cm^2, $B = 0.035$. These parameter match the data over the non-relativistic range. E is the beam energy in electron volts.

7.5 Results and Discussion.

Figures 19 (a), (b) and **(c)** show the resulting visualizations for simulations of 20 keV, 50 keV and 100 keV beam fluorescence distributions for the gas flow number density distribution given by equation (65). Parameter values for the photometric analysis listed in Table I on page 5 are assumed. for the optical system, beam and gas. The flow centerline crosses the beam axis at right angles at 25.2 cm. The axial scale is shown in the figures, the total horizontal dimension of the pictures being 50.4 cm, the vertical, 5.7 cm. The colors represent intensity bands of equal size on a logarithmic scale. Hence red represents intensities between the peak value for a given simulation down to 1/e of the peak, yellow represents values from 1/e down to $1/e^2$ of the peak, and so on. Below $1/e^6$ all intensities are mapped to black.

The peak photon count rate for the 20 keV simulation was 4.55×10^7 sec^{-1} at the beam centerline approximately 1.8 cm from the point of entry of the beam into the gas. Clearly, there is considerable beam divergence, as expected from earlier discussion. Measurable fluorescence would most likely not be seen, from primary excitation at least, beyond about 30 cm from the entry point. Even beyond 10 cm, spatial and temporal resolution of fluorescence signal becomes so poor that the beam is probably useless except for flow averaged measurements. The 50 keV simulation exhibits somewhat better penetration, though the peak photon count rate is slightly lower, 2.64×10^7 sec^{-1} at 2.8 cm, than the 20 keV simulation (consistent with equation (72)). 100

keV exhibits the least divergence, at least reaching the flow centerline with a narrow distribution above $1/e^3$ of the peak count rate, which is 1.98×10^7 sec^{-1} at 6.0 cm. The non-dimensional target thicknesses for the 20, 50 and 100 keV simulations are 84.5, 29.3 and 10.4, respectively, implying the distributions are due to predominantly multiply-scattered primary electrons.

In **Figures 20 (a), (b)** and **(c)**, the same three beam energies and photometric parameters are used, but the flow number density has been diminished to 1/10th the distribution in equation (65). Somewhat surprisingly, the highest three fluorescence bands appear only to about double or triple in length. The target thicknesses are 1/10th their above values, however, implying that the 20 keV simulation is still dominant by multiple scattering, whereas the 50 and 100 keV have significant unscattered and singly-scattered primary populations. The peak photon count rate for the 20 keV simulation was 7.99×10^6 sec^{-1} at the beam centerline approximately 1.9 cm from the beam entry point, suggesting that the beam still does not extend significantly into the core flow. The peak count rate for the 50 keV beam was 5.16×10^6 sec^{-1} at 5.8 cm, about double the distance obtained for the higher flow density. The peak count rate for the 100 keV beam was 4.22×10^6 sec^{-1} at 9.5 cm.

The significance of these results for application to two and three dimensional flow field mapping is that energies of at least 100 keV would be necessary for the high density flow, and spatially well-resolved data would be available only to the flow centerline at best. The presence of secondary electron fluorescence, which the current simulation does not model, would probably significantly degrade resolution of flow features near the centerline unless the beam were operated in pulsed mode or at significantly higher energy. Lower flow densities could be mapped with better spatial resolution, but require longer signal integration times for a specified signal-to-noise ratio.

References

[1] Muntz, E. P., "The Electron Beam Fluorescence Technique," AGARDograph, Vol. 132, Von Karman Institute, Rhode St. Genese, Belgium (1965).

[2] *Rarefied Gas Dynamics*, ed. A. E. Beylich,VCH Verlagsessellschaft mbH, Weinheim, Germany (1990), (Publication of the Proceedings of the 17th Rarefied Gas Dynamics Symposium and references to publications of prior Symposia).

[3] Cattolica, R. J., "Electron-Beam Fluorescence Measurements in Hypersonic Flows," von Karman Institute for Fluid Dynamics, Lecture Series 1990-05, 28 May - 1 June 1990, Rhode-Saint-Genese, Belgium.

[4] Dankert, C., Cattolica, R., and Sellers, W., " Local Measurements of Temperature and Concentrations: A Review for Hypersonic Flows," AGARD Fluid Dynamics Panel symposium on "Theoretical and Experimental Methods in Hypersonic Flows," May 4-8, 1992, Torino, Italy.

[5] R. J. Cattolica, "Modern Developments in Electron-Beam Fluorescence," in Rarefied Gas Dynamics, *Rarefied Gas Dynamics*, ed. A. E. Beylich,VCH Verlagsessellschaft mbH, Weinheim, Germany (1990), pp. 1581 -1592.

[6] Cattolica, R. J., Schmitt, R. L., and Palmer, R. E., "Feasibility of Non-Intrusive Optical Diagnostic Measurements in Hypersonic Boundary Layers for Flight Experiments", AIAA-90-0627 (1990).

[7] Camac, M., "Boundary Layer Measurements with an Electron Beam", AVCO Everett Research Rept. 275 (1967).

[8] Center, R. E., "Plural and Multiple Scattering of Fast Electrons in Gases", Phys. Fluids 13, No. 1 (1970) 79-88.

[9] Bogdan, L., and McCaa, D. J., "Experimental Study of Electron-Excited Emission in Air and in Nitrogen up to 8 torr", Cornell Aeronautical Rept. CAL-AG-2679-Y-1 (1970).

[10] Cunningham, J. W., Fisher, C. H., and Price, L. L., IEEE Trans. Aerospace Electron. Systems 3 (1967) 269.

[11] Petrie, S. L., and Boiarski, A. A., "The Electron Beam Diagnostic Technique for Rarefied Gas Flows at Low Static Temperatures", in Rarefied Gas Dynamics 6th Int. Symp. (L. Trilling, and H. Y. Wachman, eds.), Supp. 5, Vol. II, Academic Press (1969), 1685-1702.

[12] Borst, W. L., and Imami, M., "Production of Secondary Electrons in Nitrogen by Fast Electrons and Simultaneous Excitation of N_2 Bands", J. Appl. Phys. 44 (1973), 1133-1141.

[13] Rebrov, A. K., Karelov, N. V., Sukhinin, G. I., Sharafutdinov, R. G., and Lengrand, J. C., "Electron Beam Diagnostics in Nitrogen: Secondary Processes", in Rarefied Gas Dynamics,Part II. (S. Fisher ed.), AIAA Progress in Aeronautics and Astronautics Vol. 74 (1980) 931-945.

[14] Lengrand, J.-C., Allegre, J., and Raffin, M., "Electron Beam Fluorescence Technique at Relatively High Density", in Rarefied Gas Dynamics 14th Int. Symp. (H. Oguchi, ed.), Vol. I, University of Tokyo Press (1984), 423-429.

[15] Jacob, J. H., "Multiple Electron Scattering through a Slab", Phys. Rev. A 8, No. 1 (1973) 226-235.

[16] Harbour, P. J., Bienkowski, G. K., and Smith, R. B., "Influence of Secondary Electrons on an Electron-Beam Probe", Phys. Fluids 11, No. 4 (1968) 800-803.

[17] Lee, E. P.and Cooper, R. K., "General Envelope Equation for Cylindrically Symmetric Charged-Particle Beams", Particle Accelerators 7 (1976) 83.

[18] Vest, C. M., Holographic Interferometry, J. Wiley and sons, New York (1979)

[19] Cremers, C. J.and Birkebak, R. C., "Application of the Abel Integral Equation to Spectrographic Data", Appl. Opt. 5, No. 6 (1966) 1057-1064.

[20] Maguire, B. L., "The Effective Spatial Resolution of the Electron Beam Technique in Helium", in *Rarefied Gas Dynamics*, Supp. 4, Vol.2 (C. Brundin, ed.), Academic Press (1967).

[21] Gordon, R. "A tutorial on ART", IEEE Trans. Nucl. Sci NS-21 (1974) 78.

[22] Hughey, B. J.and Santavicca, D. A., "A Comparison of Techniques for Reconstructing Axisymmetric Reacting Flow Fields from Absorption Measurements," Combustion Sci. and Tech. 29 (1982) 167-190.

[23] Mott, N. F.and Massey, S. W., *Theory of Atomic Collisions*, Oxford Univ. Press (1949).

[24] Scott, W. T., "Theory of Small-Angle Multiple Scattering of Fast Charged Particles," Rev. of Modern Physics, 35, (1963) 231-313.

[26] Cattolica, R.J., Clapp, L. H., and Twiss, R.G., "Characterization of Electron Beam Propagation for Hypersonic Flight Research Applications", AIAA 4th Int. Symp., Aerospace Plances Conf. (1992).

[27] Berkes, I, Demeter, I., Nucl. Phys. **15** (1960) 421.

[28] Lenz, F., Z. Naturforsch. 9a (1954) 185.

[29] Ibers, J. A., *International Tables for X-Ray Crystallography*, Vol. III, Kynoch Press, Birmingham, England (1962) 201.

[30] Motz, J.W., Olsen, H., Koch, H.W., Rev. Mod. Phys. **36** (1964) 881.

[31] Bethe, H. A., Ashken, J., in *Experimental Nuclear Physics, Vol. 1*, E. Segre, Ed., John Wiley, New York (1953) 253.

[32] Lewis, J.W.L., Rarefied Gas Dynamics, AIAA pub. (1989) 107-132.

[33] Rossi, B. B., Greisen, K. I., Rev. Mod. Phys. **13** (1941) 240.

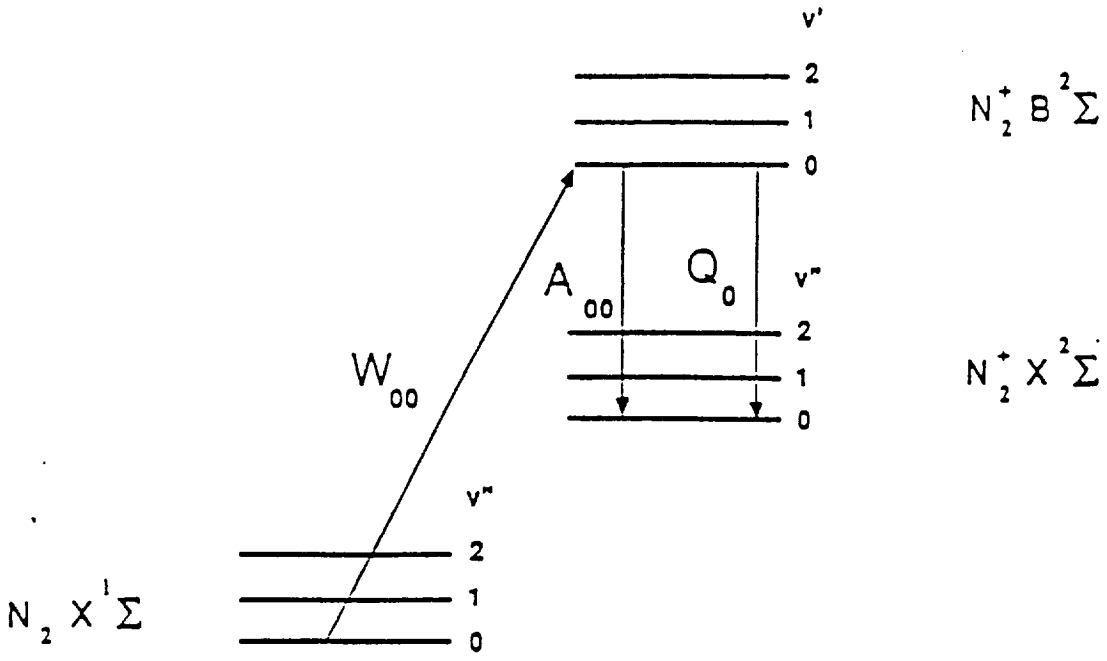

Figure 1. Electron-beam fluorescence excitation and emission scheme for nitrogen.

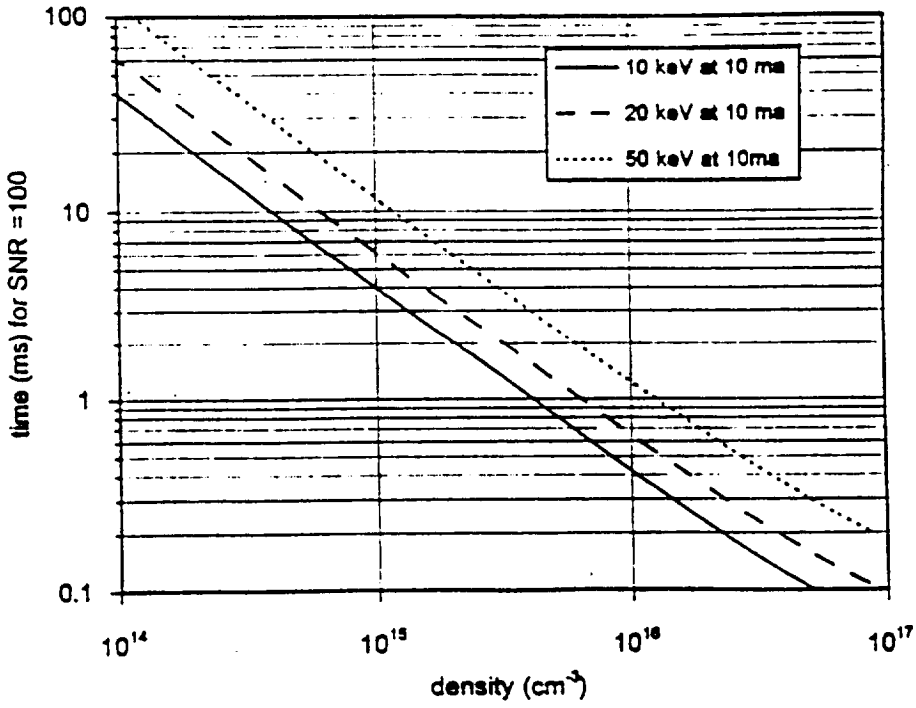

Figure 2. Signal integration time required to maintain a signal-to-noise ratio (SNR)of 100 in the measurement of nitrogen density from the electron-beam fluorescence (at 391.4nm) from $N_2^+(0,0)$ band of the $B\,^2\Sigma$ -$X\,^2\Sigma$ transition as a function of the gas density for three electron energies: 10 keV, 20 keV, and 50 keV.

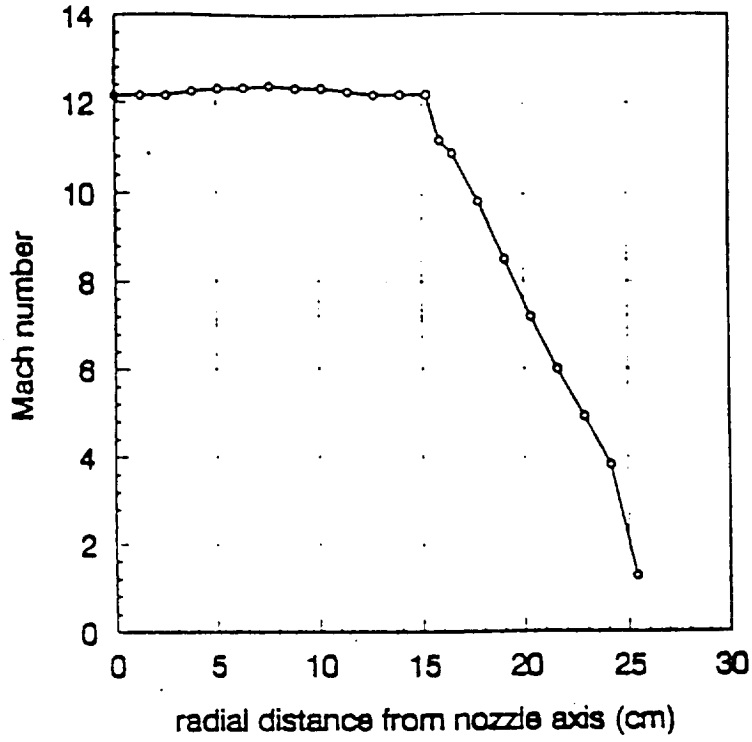

Figure 3. Radial distribution of Mach number across a 20-inch Mach-12 nozzle in a hypersonic wind tunnel.

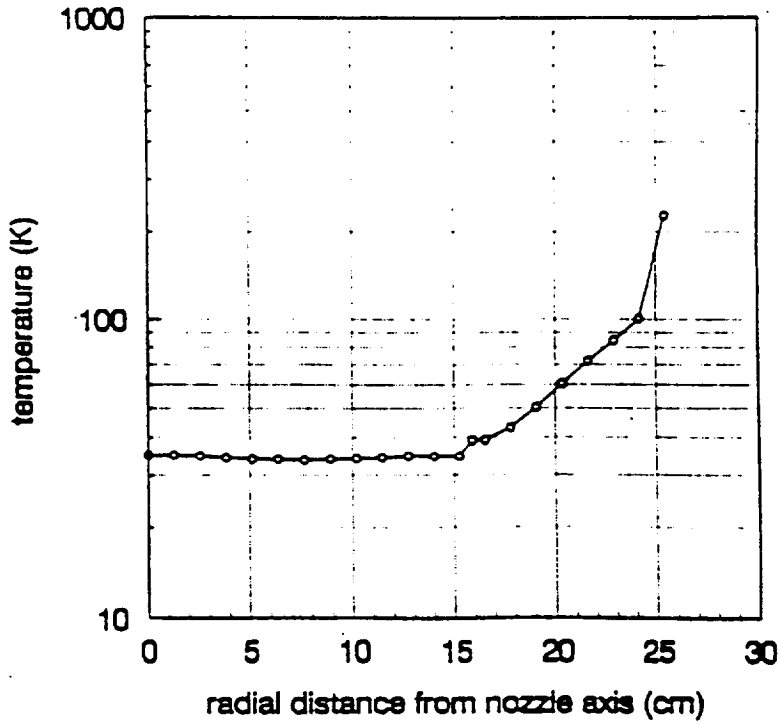

Figure 4. Radial distribution of temperature across a 20-inch Mach-12 nozzle in a hypersonic wind tunnel.

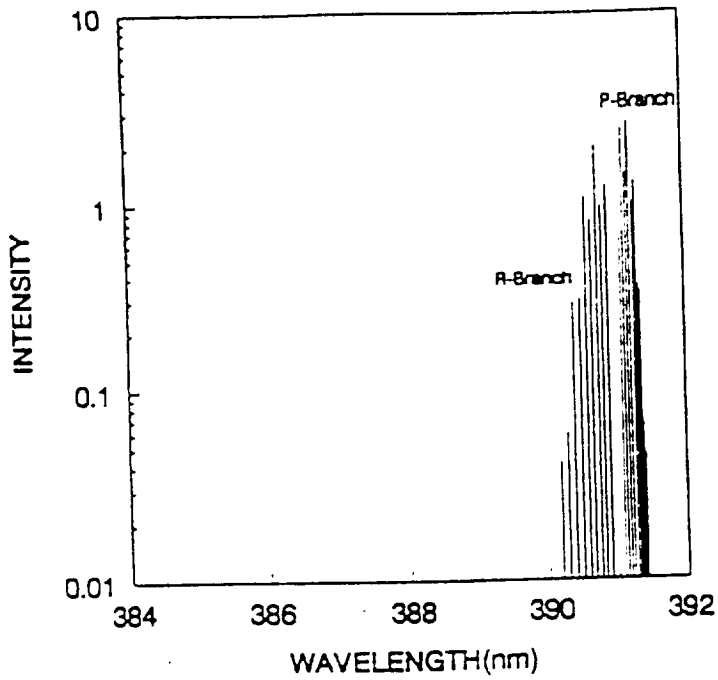

(a)

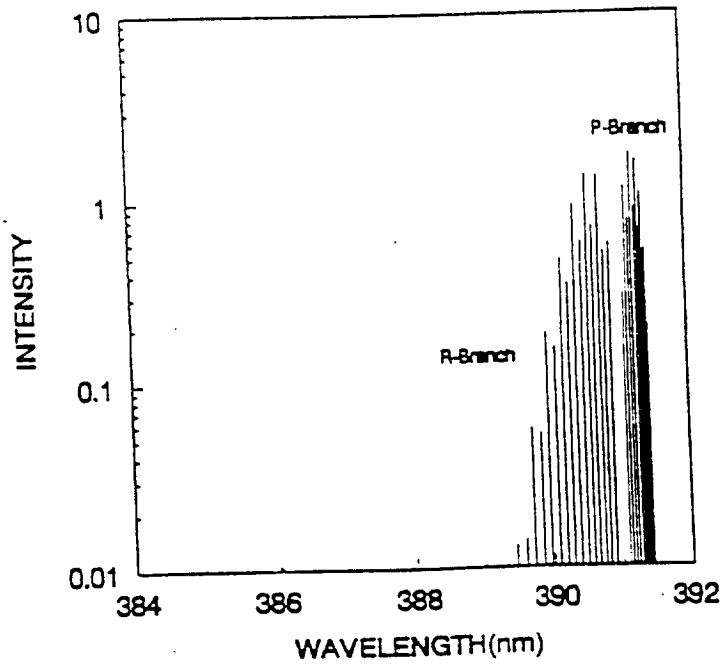

(b)

Figure 7. Calculated rotational spectra for the electron-beam fluorescence from the nitrogen first-negative band [$N_2^+B\ ^2\Sigma_u^+ \rightarrow N_2^+X\ ^2\Sigma_g^+$] at different temperatures: **(a)** 40 K, **(b)** 100 K, **(c)** 200 K, **(d)** 400 K, **(e)** 700 K, **(f)** 1000K.

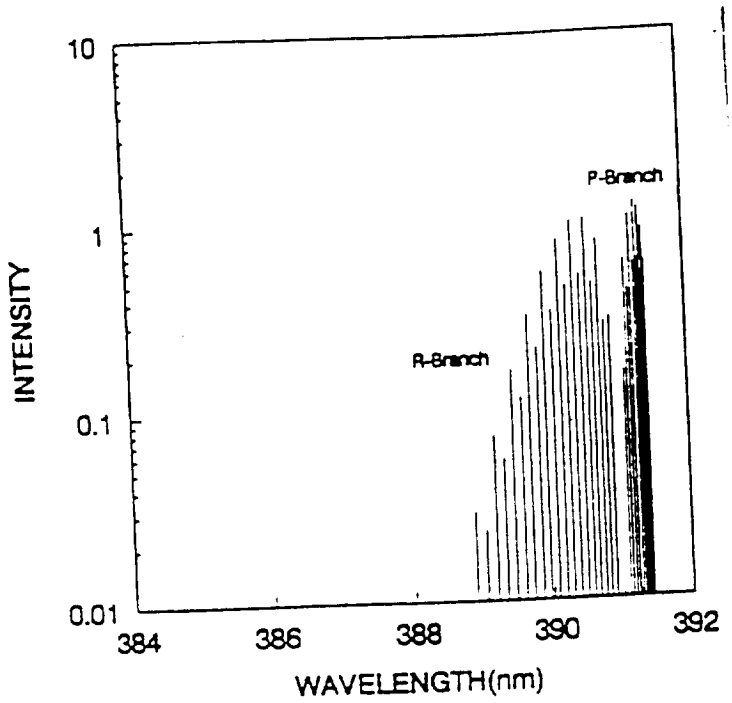

(c)

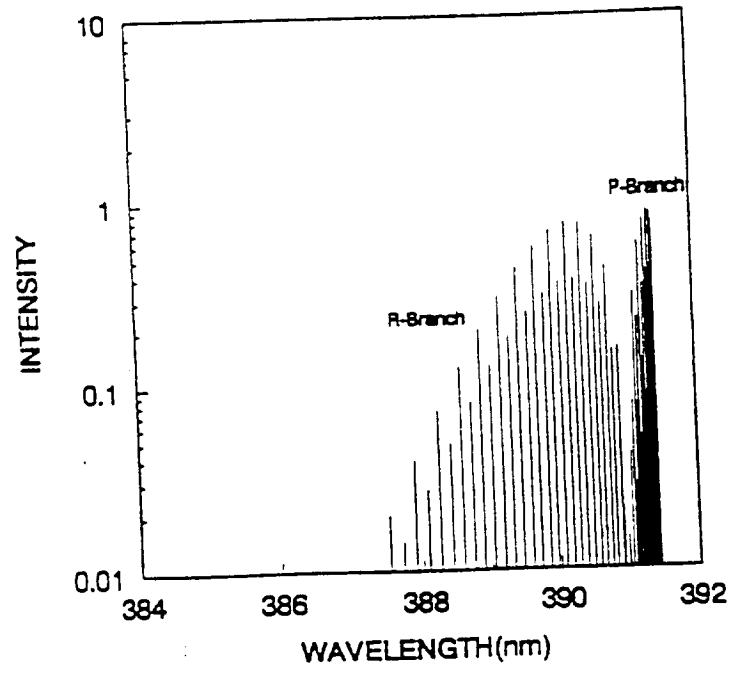

(d)

Figure 7. Calculated rotational spectra for the electron-beam fluorescence from the nitrogen first-negative band [$N_2^+B\ ^2\Sigma_u^+ \rightarrow N_2^+X\ ^2\Sigma_g^+$] at different temperatures: **(a)** 40 K, **(b)** 100 K, **(c)** 200 K, **(d)** 400 K, **(e)** 700 K, **(f)** 1000K.

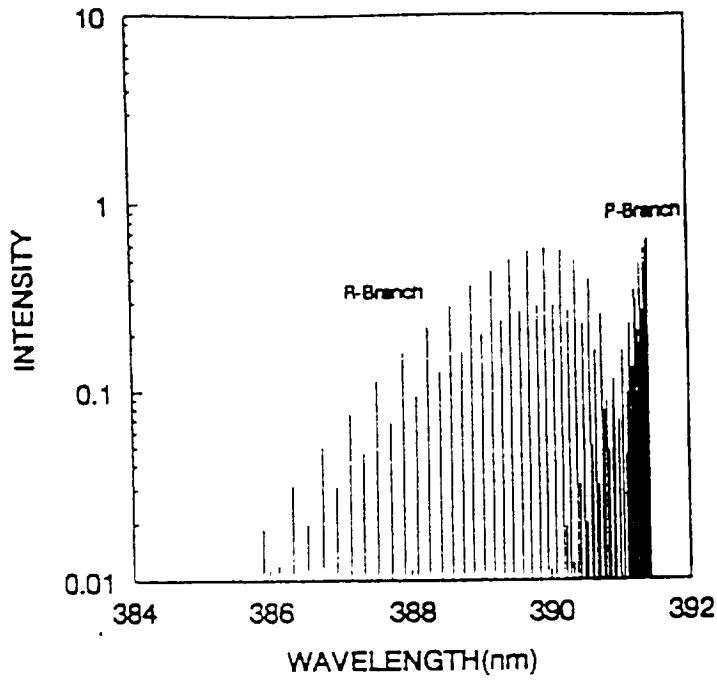

(e)

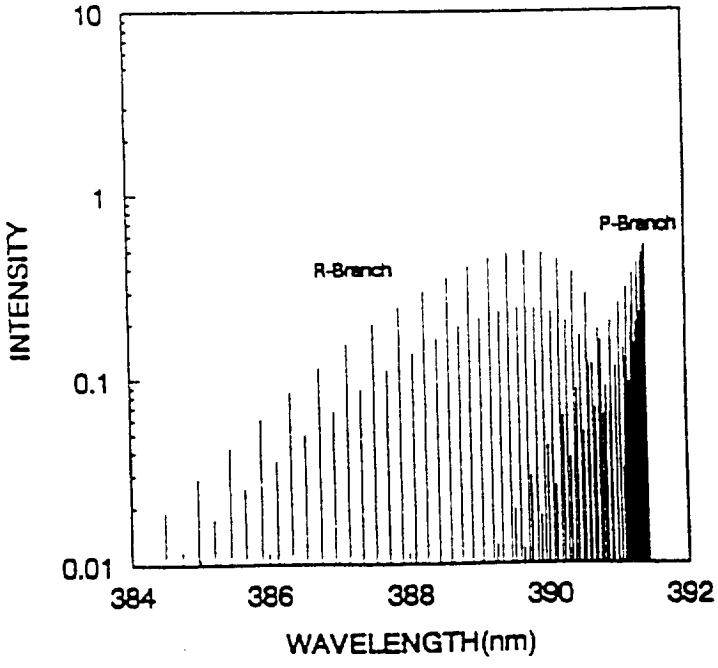

(f)

Figure 7. Calculated rotational spectra for the electron-beam fluorescence from the nitrogen first-negative band [$N_2^+B\ ^2\Sigma_u^+ \rightarrow N_2^+X\ ^2\Sigma_g^+$] at different temperatures: **(a)** 40 K, **(b)** 100 K, **(c)** 200 K, **(d)** 400 K, **(e)** 700 K, **(f)** 1000K.

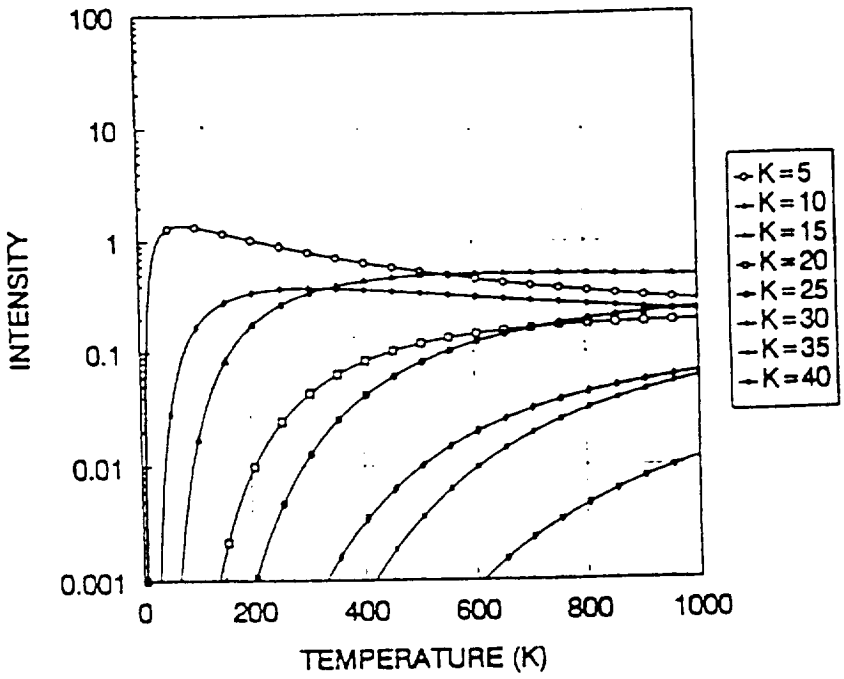

Figure 8. Variation of signal intensity from rotational transitions in the electron-beam fluorescence from the nitrogen first-negative band [$N_2^+B\ ^2\Sigma_u^+ \rightarrow N_2^+X\ ^2\Sigma_g^+$] as a function of temperature.

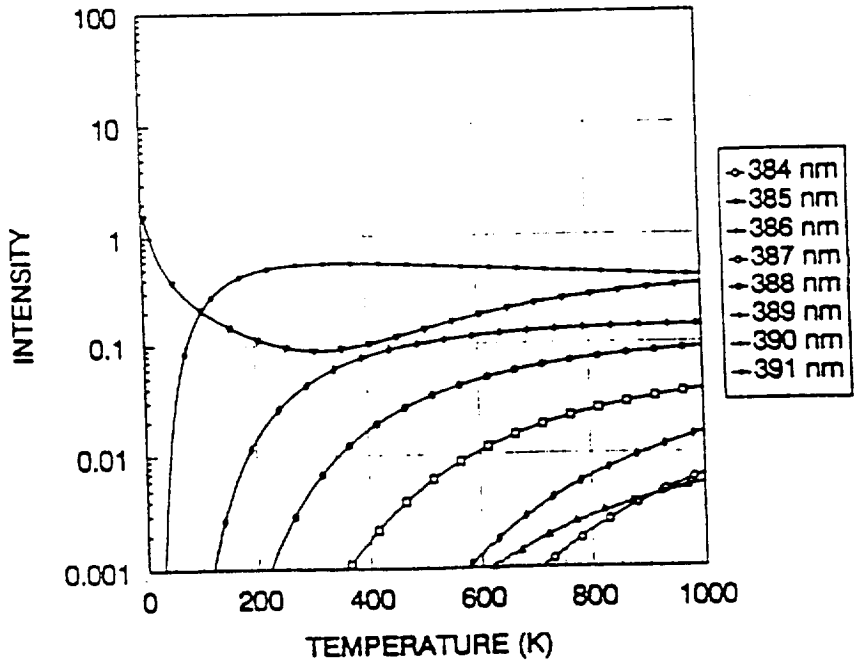

Figure 9a. Relative signal intensity of the electron-beam fluorescence from the nitrogen first-negative band [$N_2^+B\ ^2\Sigma_u^+ \rightarrow N_2^+X\ ^2\Sigma_g^+$] using a band pass filter (0.1-nm bandwidth) at various center wavelengths as a function of temperature.

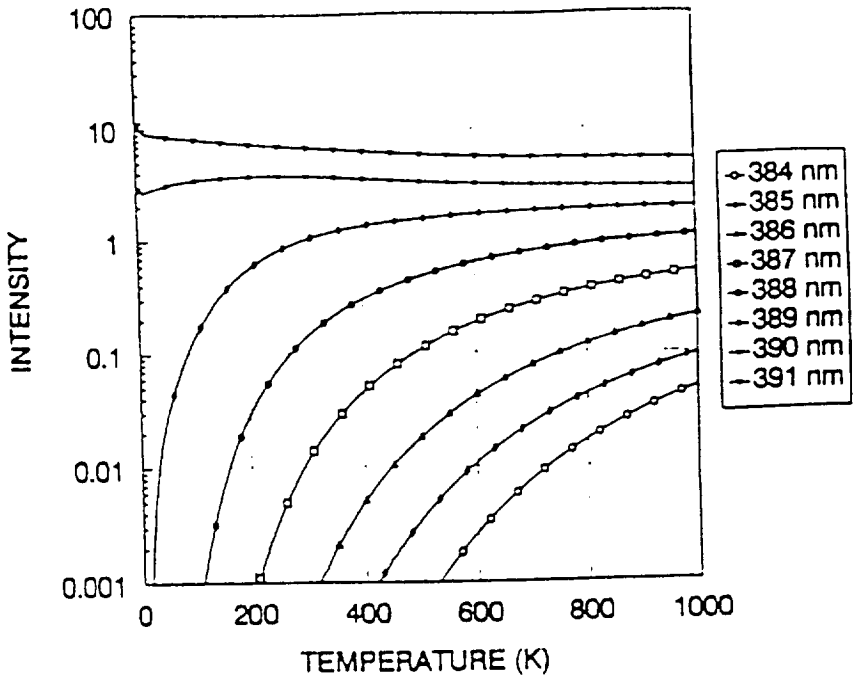

Figure 9b. Relative signal intensity of the electron-beam fluorescence from the nitrogen first-negative band [$N_2^+B\ ^2\Sigma_u^+ \rightarrow N_2^+X\ ^2\Sigma_g^+$] using a band pass filter (1.0-nm bandwidth) at various center wavelengths as a function of temperature.

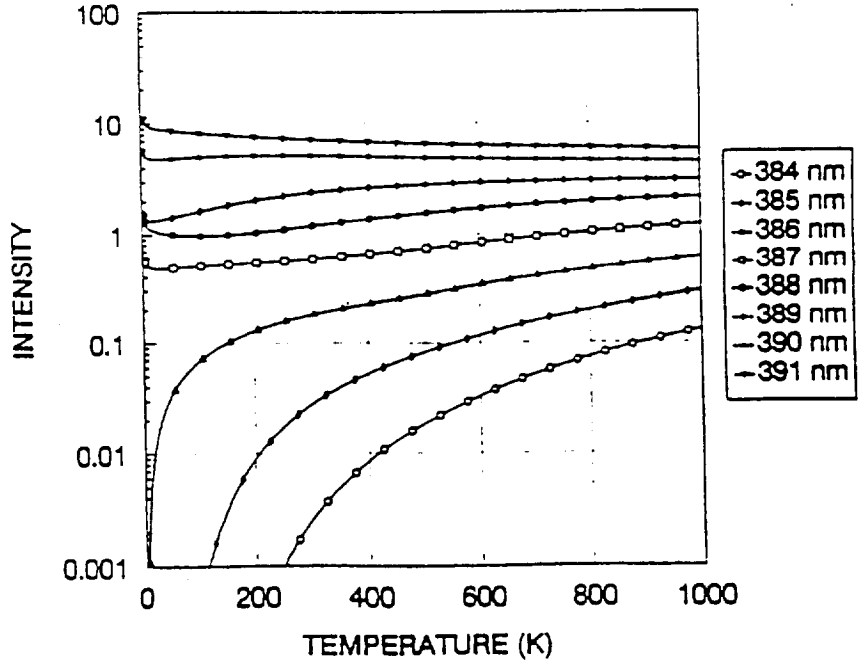

Figure 9c. Relative signal intensity of the electron-beam fluorescence from the nitrogen first-negative band [$N_2^+B\ ^2\Sigma_u^+ \rightarrow N_2^+X\ ^2\Sigma_g^+$] using a band pass filter (2.0-nm bandwidth) at various center wavelengths as a function of temperature.

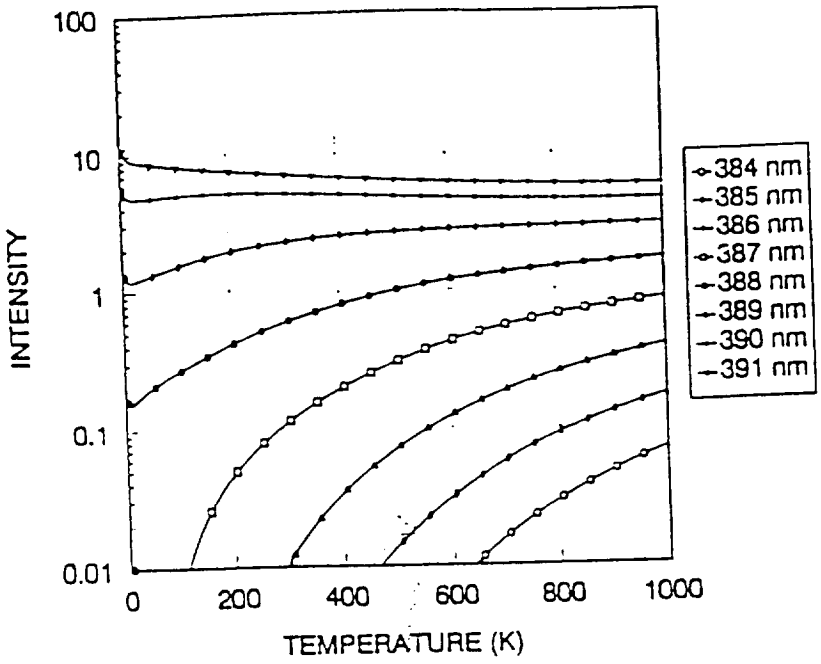

Figure 9d. Relative signal intensity of the electron-beam fluorescence from the nitrogen first-negative band [$N_2^+B\ ^2\Sigma_u^+ \rightarrow N_2^+X\ ^2\Sigma_g^+$] using a band pass filter (3.0-nm bandwidth) at various center wavelengths as a function of temperature.

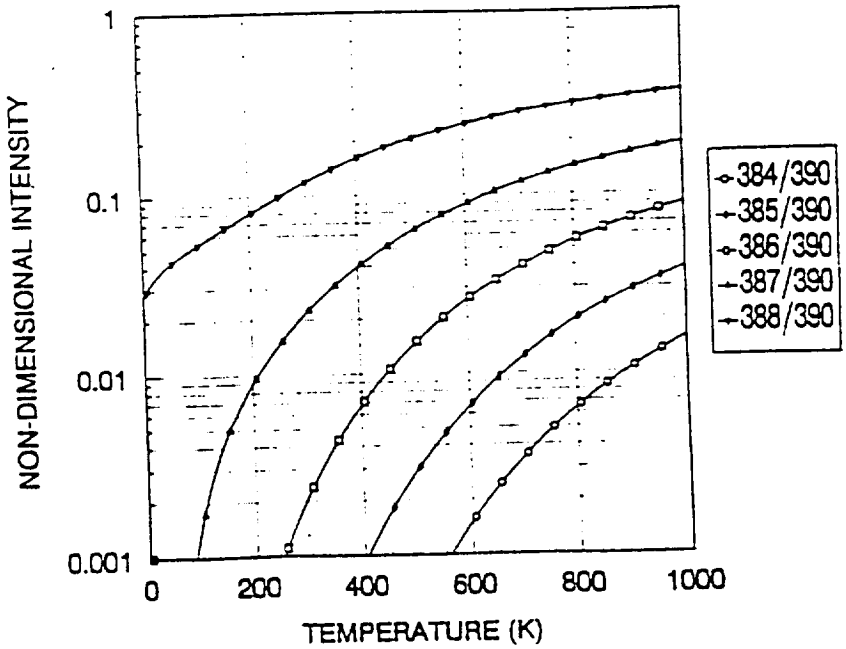

Figure 10. Signal intensity ratios of the electron-beam fluorescence from the nitrogen first-negative band [$N_2^+B\ ^2\Sigma_u^+ \rightarrow N_2^+X\ ^2\Sigma_g^+$] using a band pass filter (2.0-nm bandwidth) at center wavelengths of 384, 385, 386, 387, and 388 nm as a function of temperature. The signal intensity from a 390-nm filter is used for normalization.

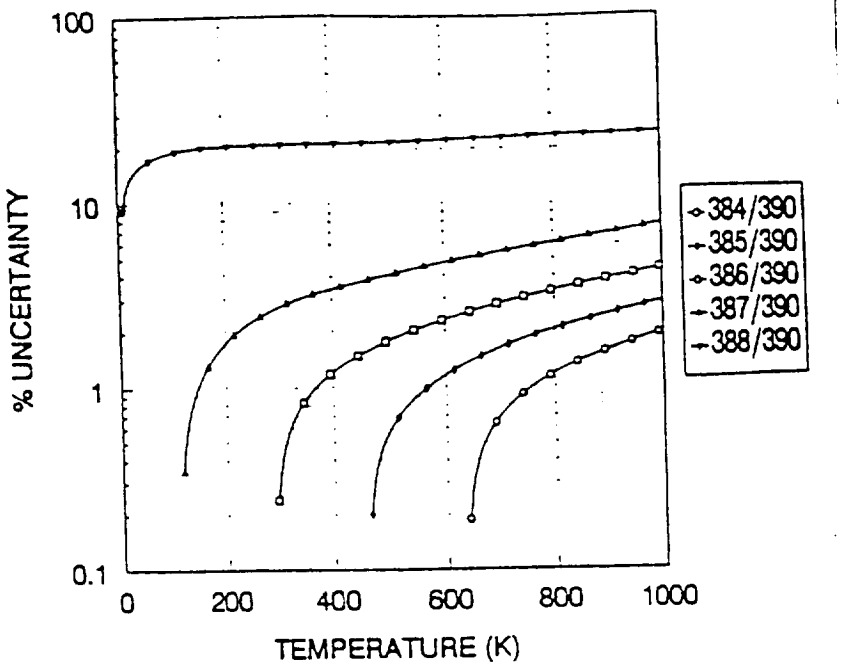

Figure 11. Precision of fluorescence temperature measurements as a function of rotational temperature from intensities ratios at 384, 385, 386, 387, and 388 nm as give in Figure 4.The precision (uncertainty) in the intensity ratio measurement is fixed at 1%.

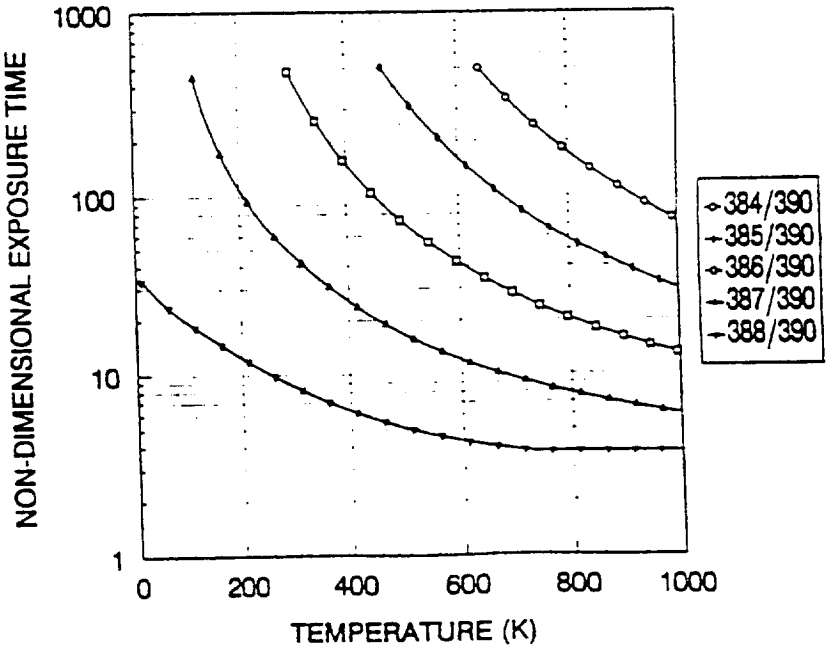

Figure 12. Relative signal acquisition time required to obtain 1% percussion in intensity ratio measurements as a function of rotational temperature. The reference time used for normalization is the time required to obtain 1% rescission in the intensity measurement from a 390-nm filter at 300 K.

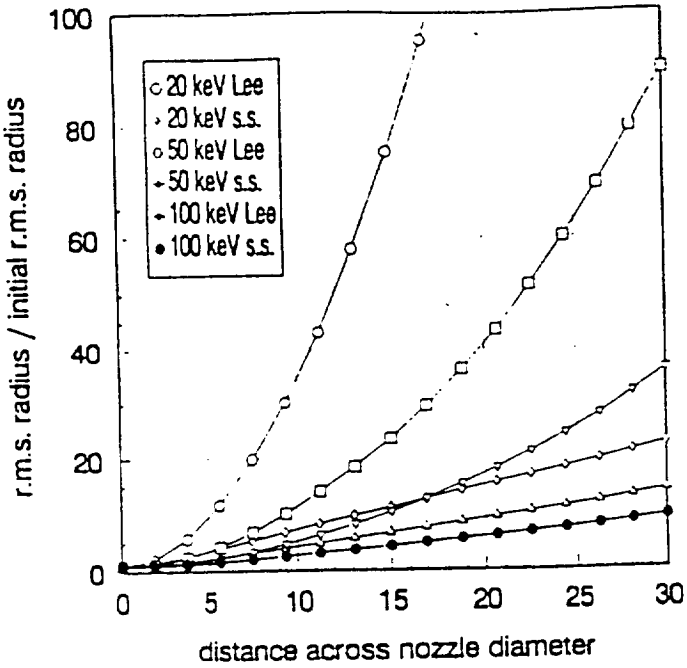

(a)

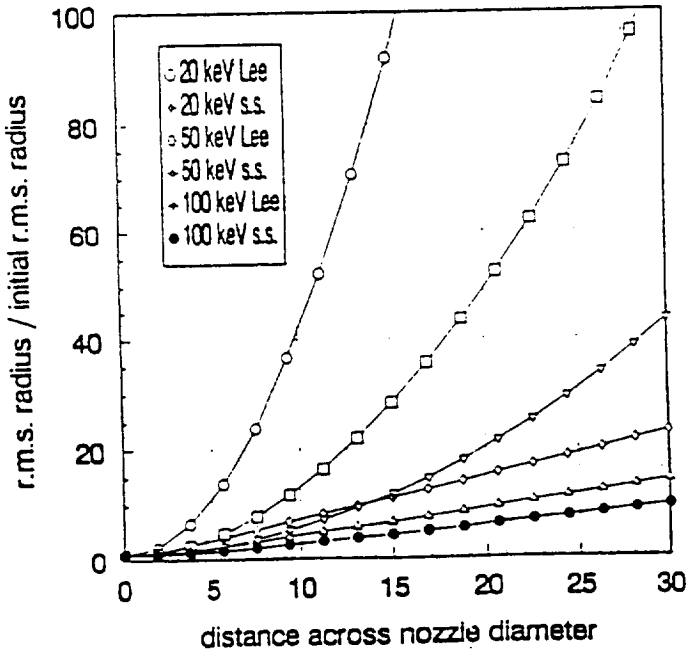

(b)

Figure 13. Calculated growth in electron beam root mean square radius across Mach 12 nozzle due to scattering at three gas pressures: **(a)** 45 atm, **(b)** 55 atm, and **(c)** 60 atm.

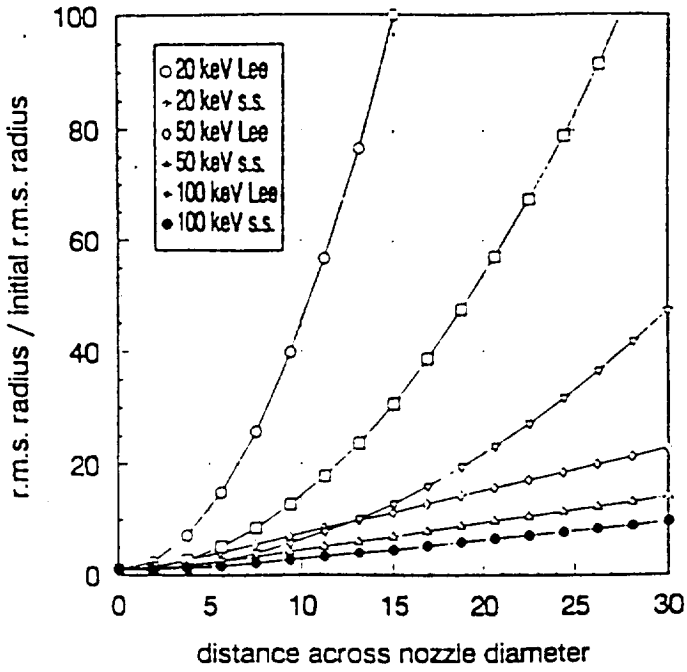

(c)

Figure 13. Calculated growth in electron beam root mean square radius across Mach 12 nozzle due to scattering at three gas pressures: **(a)** 45 atm, **(b)** 55 atm, and **(c)** 60 atm.

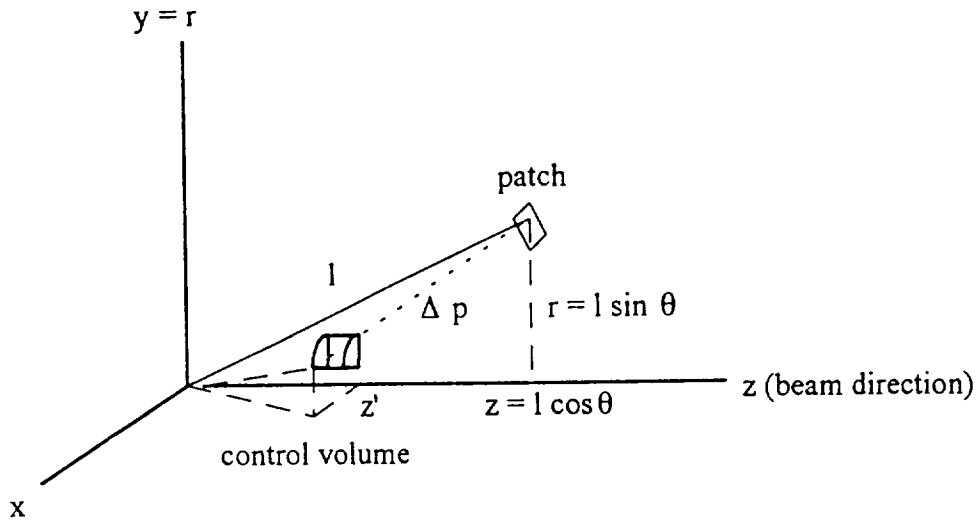

Figure 14(a): Perspective diagram of single-scattering used for calculating flux of electrons from control volume to patch.

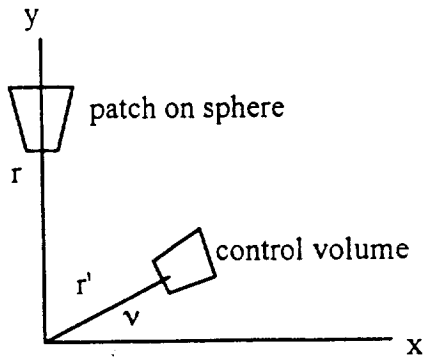

Figure 14(b): View along beam axis. Patch is further from viewer than control volume.

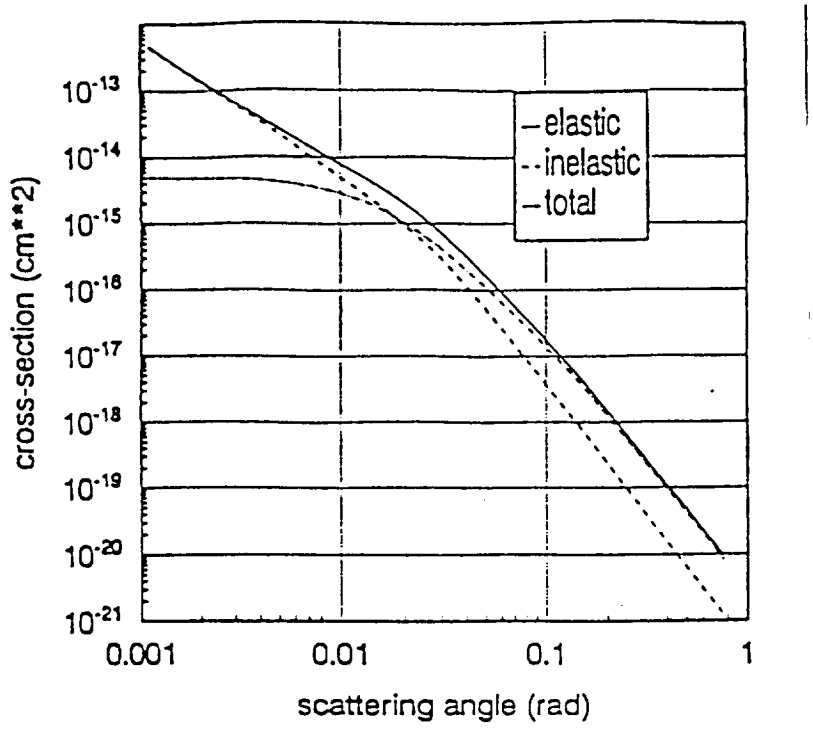

Figure 15(a): Differential cross-section computation for nitrogen, based on Center's [8] analysis. Electron energy is 20 keV.

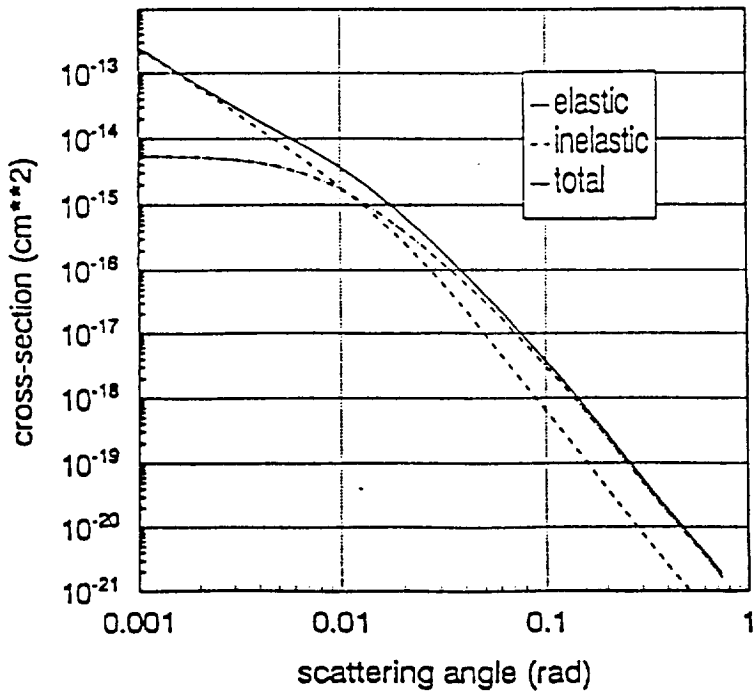

Figure 15(b): Differential cross-section computation for nitrogen, based on Center's [8] analysis. Electron energy is 50 keV.

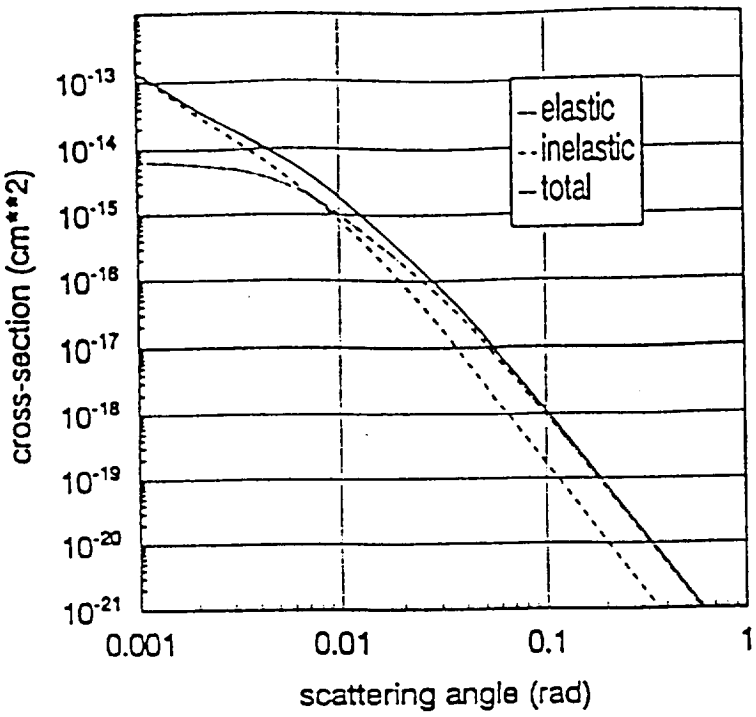

Figure 15(c): Differential cross-section computation for nitrogen, based on Center's [8] analysis. Electron energy is 100 keV.

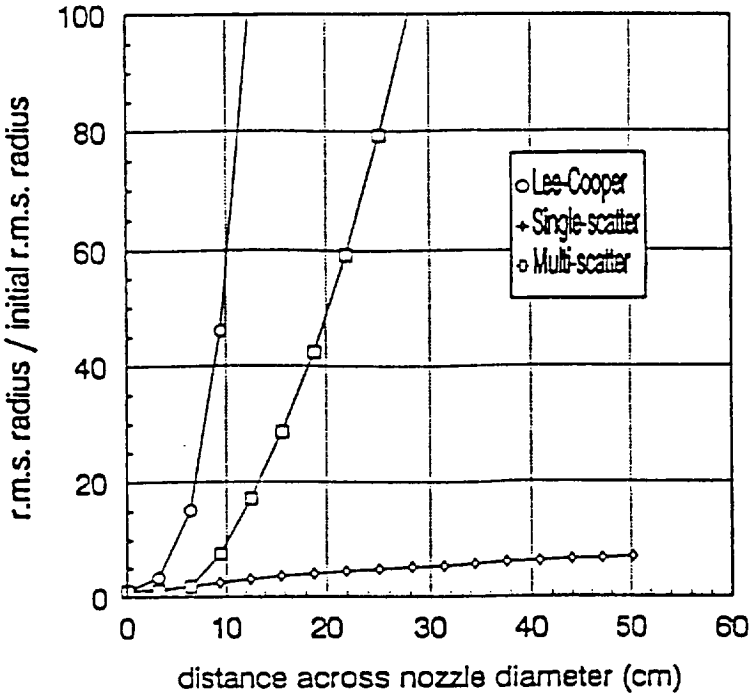

Figure 16(a): Predicted growth in electron beam root mean square radius across Mach 12 nozzle. Beam energy is 20 keV.

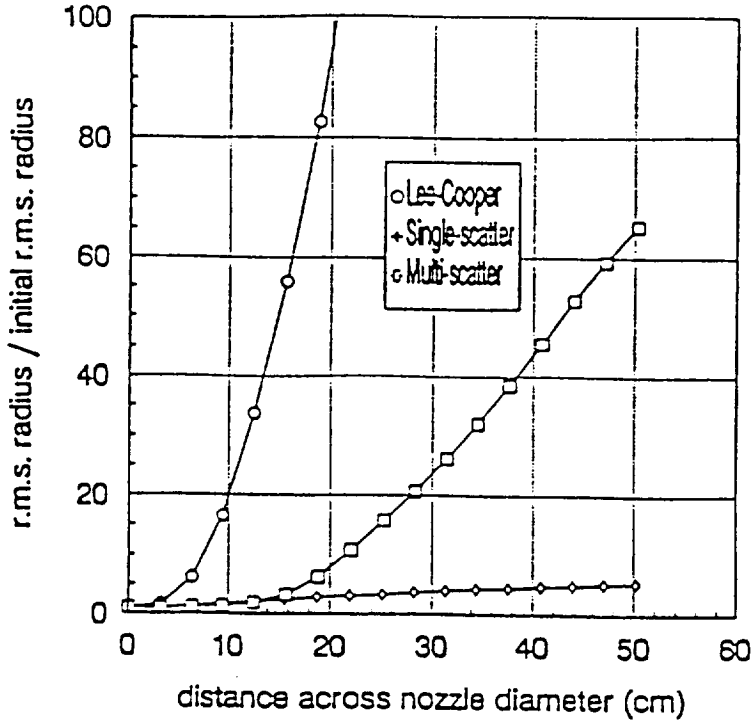

Figure 16(b): Predicted growth in electron beam root mean square radius across Mach 12 nozzle. Beam energy is 50 keV.

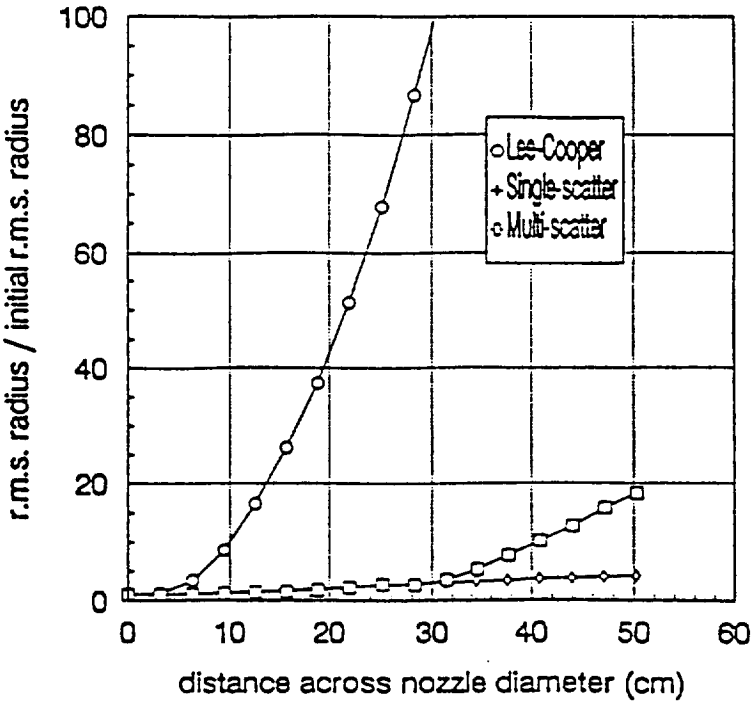

Figure 16(c): Predicted growth in electron beam root mean square radius across Mach 12 nozzle. Beam energy is 100 keV.

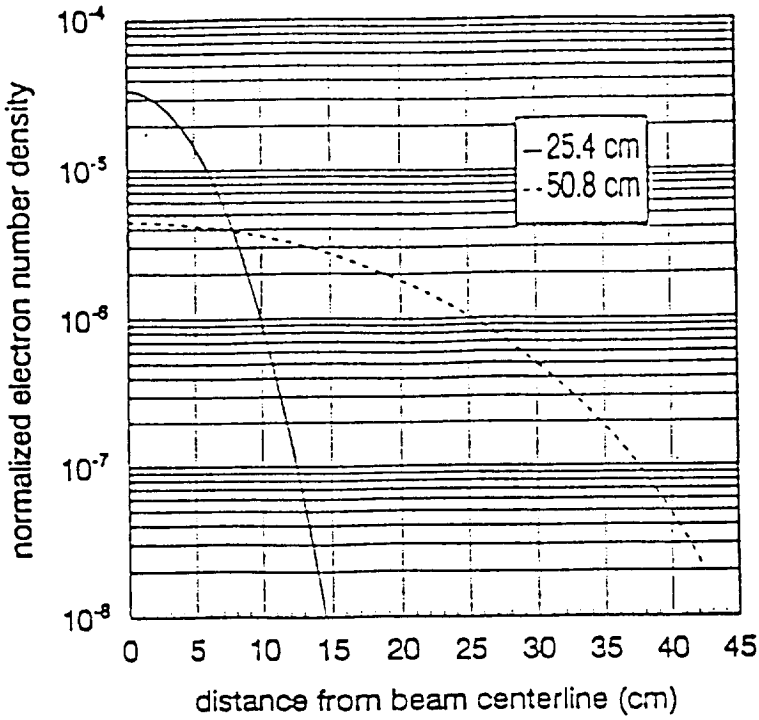

Figure 17(a): Radial electron number density distribution for a beam with an initial radius of 1 mm. Calculation is at two positions along the beam. Electron energy is 20 keV.

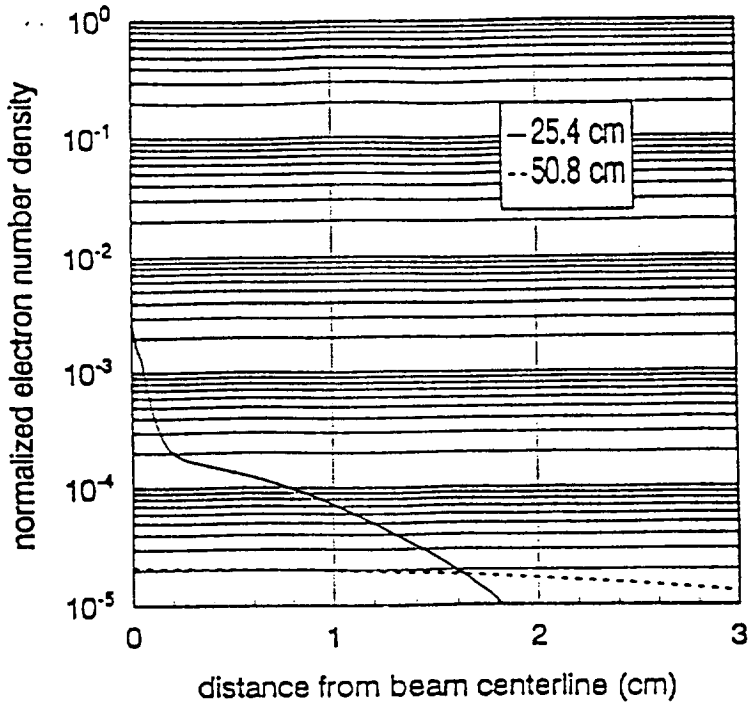

Figure 17(b): Radial electron number density distribution for a beam with an initial radius of 1 mm. Calculation is at two positions along the beam. Electron energy is 50 keV.

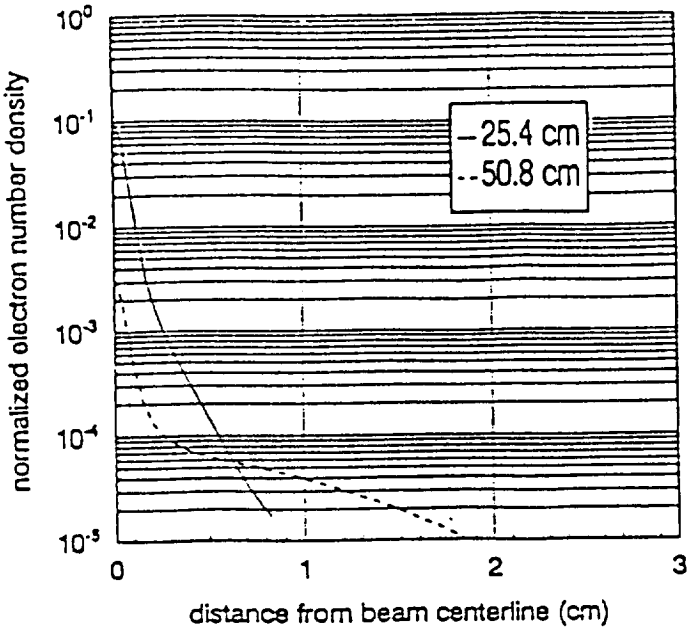

Figure 17(c): Radial electron number density distribution for a beam with an initial radius of 1 mm. Calculation is at two positions along the beam. Electron energy is 100 keV.

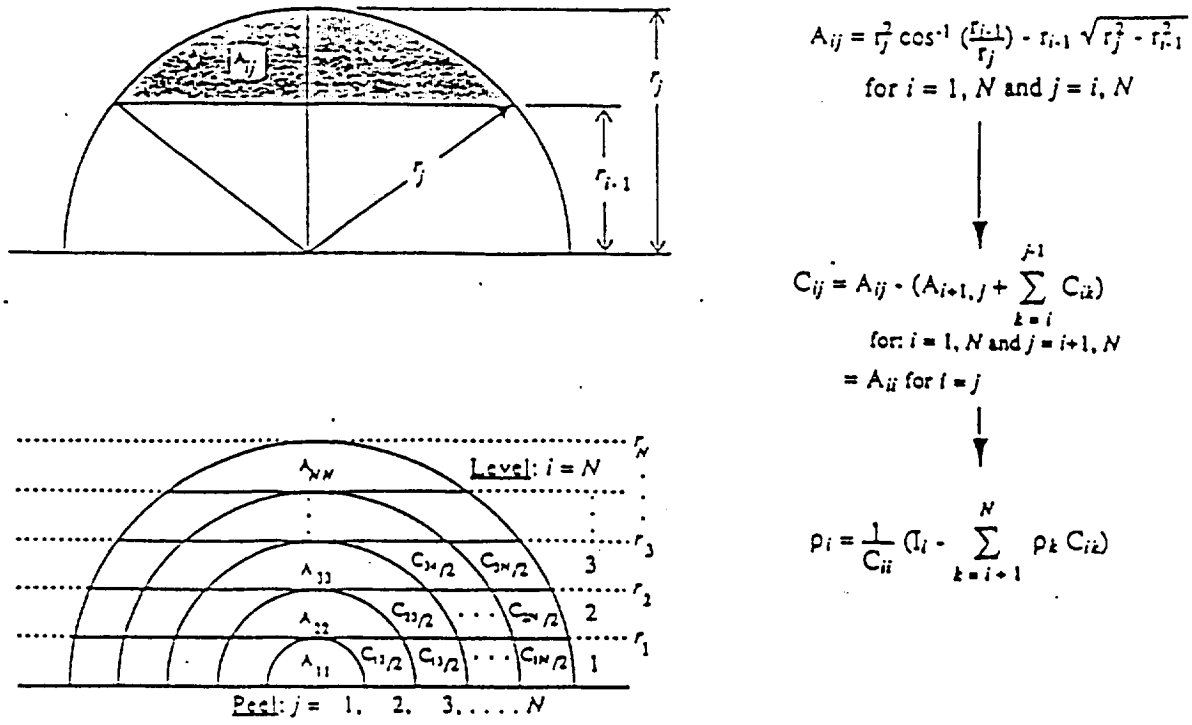

Figure 18: Projection of volumetric fluorescence emission on to an image plane.

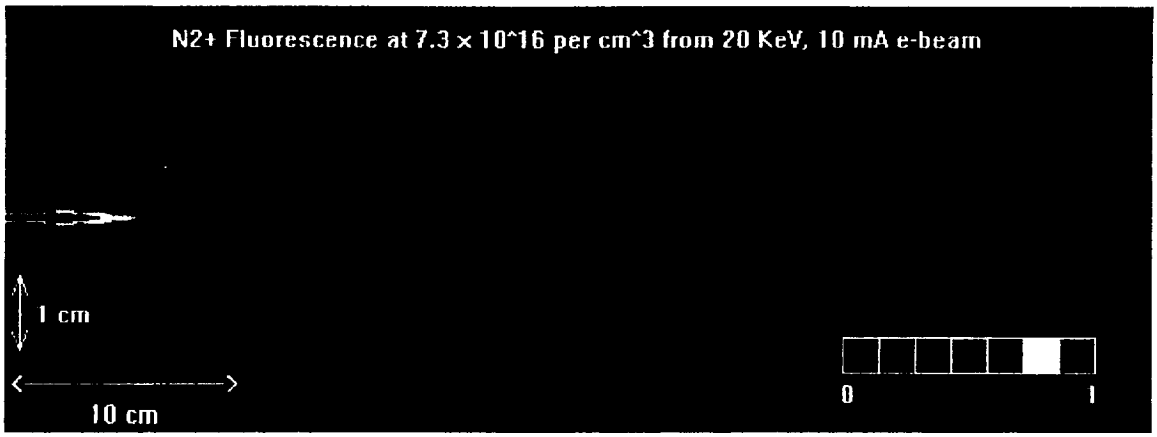

(a)

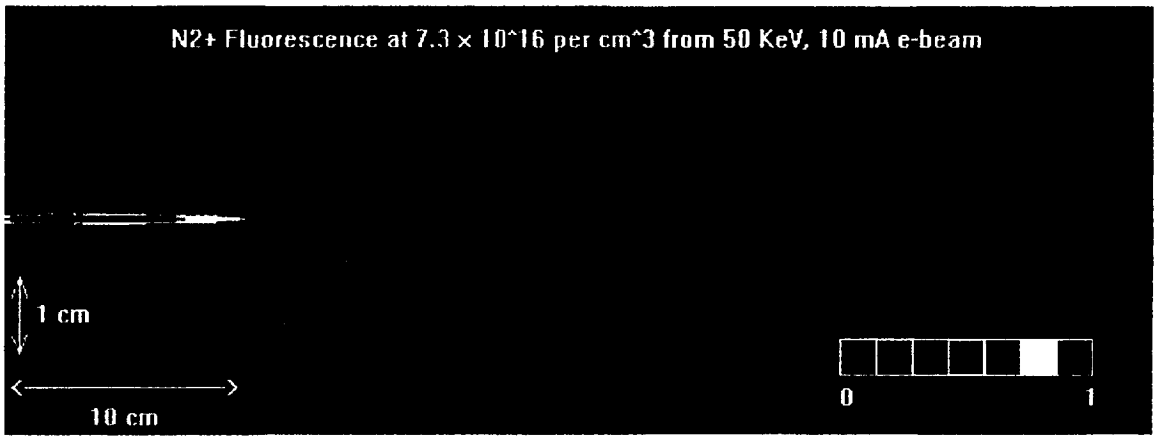

(b)

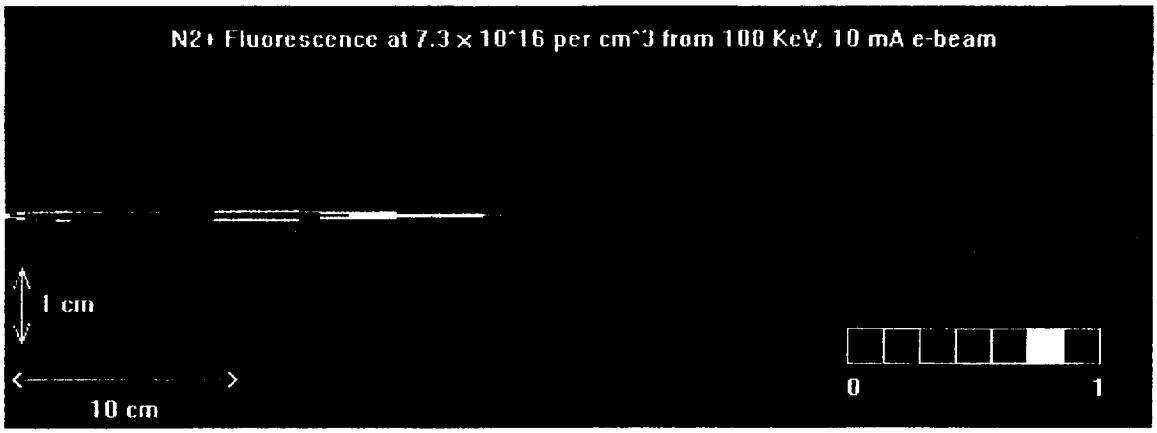

(c)

Figure 19: Simulation of $N2^+$ fluorescence distribution due to primary excitation. Electron energies are (a) 20, (b) 50 and (c) 100 KeV. Gas distribution along beam axis is given by Eq. (65).

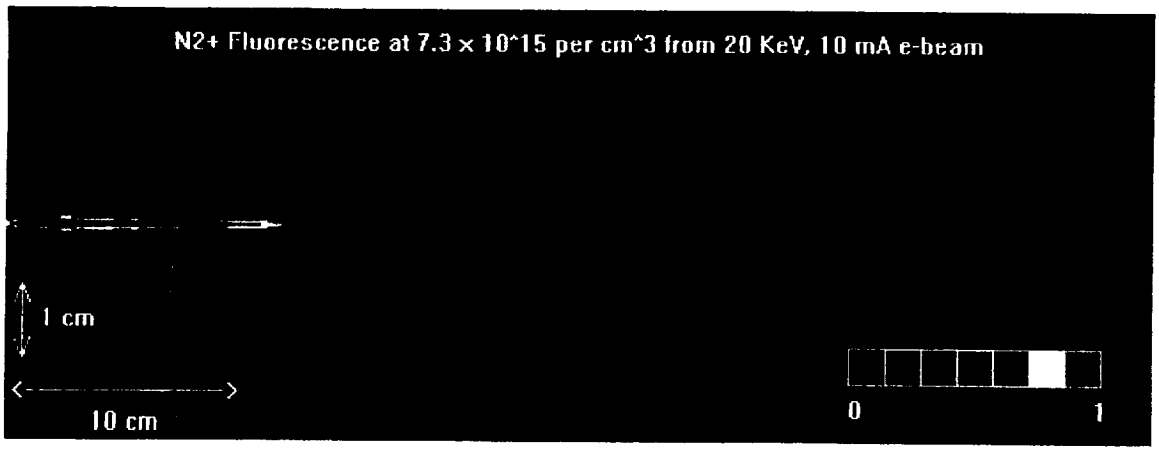

(a)

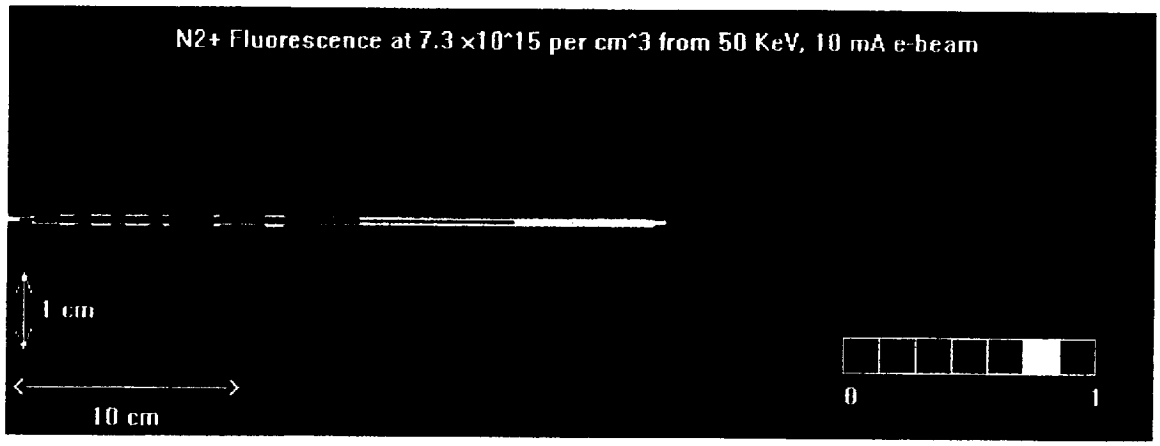

(b)

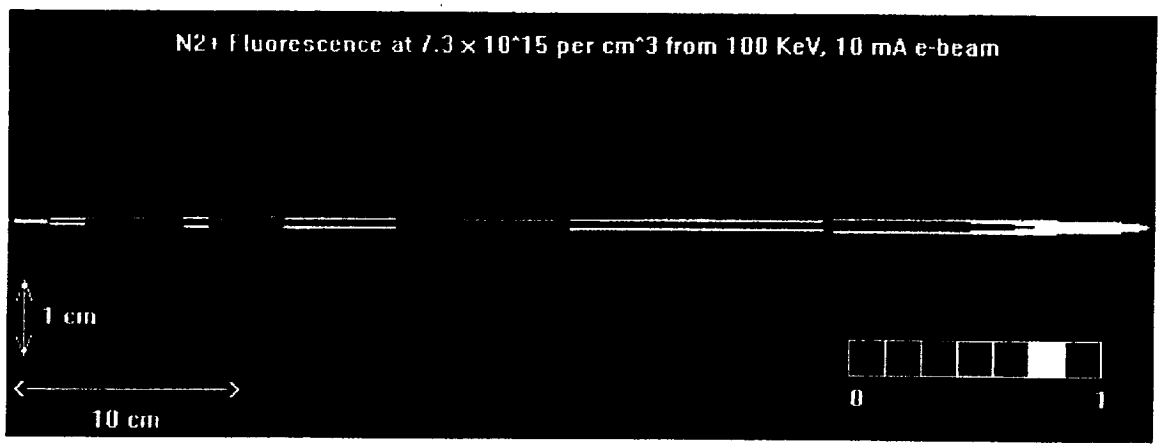

(c)

Figure 20: Simulation of N2+ fluorescence distribution due to primary excitation. Electron energies are (a) 20, (b) 50 and (c) 100 KeV. Gas distribution along beam axis is given by Eq. (65) divided by 10.